Cell

Article

A Thalamic Orphan Receptor Drives Variability in Short-Term Memory

Graphical Abstract

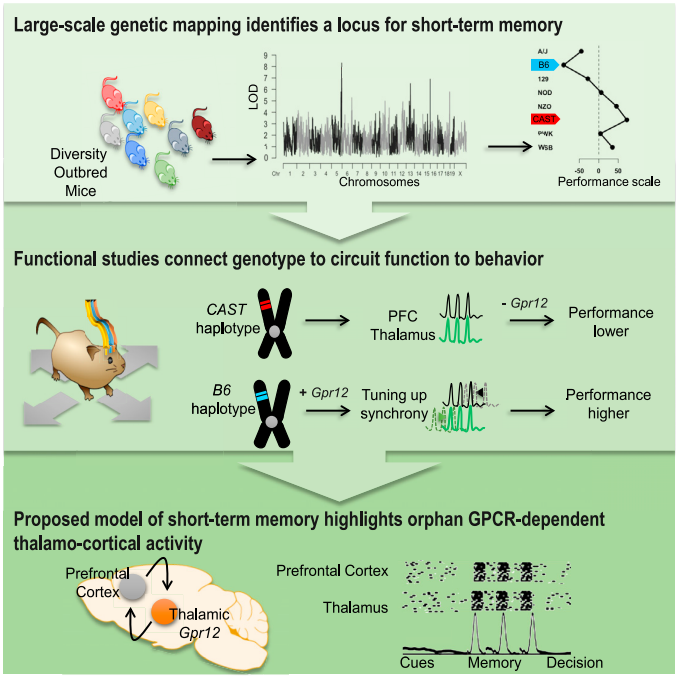

Highlights

- Genetic mapping in outbred mice identifies a locus (*Smart1*) for short-term memory
- Thalamic transcriptome stratifies *Smart1* haplotypes into high and low performers
- Within the *Smart1* locus, an orphan GPCR is a potent modifier of short-term memory
- Brain recordings reveal Gpr12-driven thalamocortical functions in short-term memory

Authors

Kuangfu Hsiao, Chelsea Noble, Wendy Pitman, ..., Ravi Tolwani, Praveen Sethupathy, Priyamvada Rajasethupathy

Correspondence

pr46@cornell.edu (P.S.), priya@rockefeller.edu (P.R.)

In Brief

A modifier of short-term memory, the orphan receptor *Gpr12* is identified using genetic mapping in outbred mice and characterized to reveal that it enables thalamus-PFC synchrony to support memory maintenance and choice accuracy.

Hsiao et al., 2020, Cell *183*, 1–15
October 15, 2020 Published by Elsevier Inc.
https://doi.org/10.1016/j.cell.2020.09.011

Please cite this article in press as: Hsiao et al., A Thalamic Orphan Receptor Drives Variability in Short-Term Memory, Cell (2020), https://doi.org/10.1016/j.cell.2020.09.011

Cell

CellPress

Article

A Thalamic Orphan Receptor Drives Variability in Short-Term Memory

Kuangfu Hsiao,[1] Chelsea Noble,[1,5] Wendy Pitman,[2,5] Nakul Yadav,[1] Suraj Kumar,[1] Gregory R. Keele,[3] Andrea Terceros,[1] Matt Kanke,[2] Tara Conniff,[1] Christopher Cheleuitte-Nieves,[4] Ravi Tolwani,[4] Praveen Sethupathy,[2,*] and Priyamvada Rajasethupathy[1,*]

[1]Laboratory of Neural Dynamics & Cognition, The Rockefeller University, New York, NY 10065, USA
[2]Department of Biomedical Sciences, Cornell University, Ithaca, NY 14853, USA
[3]The Jackson Laboratory, Bar Harbor, ME 04609, USA
[4]Comparative Bioscience Center, The Rockefeller University, New York, NY 10065, USA
[5]These authors contributed equally
*Correspondence: pr46@cornell.edu (P.S.), priya@rockefeller.edu (P.R.)
https://doi.org/10.1016/j.cell.2020.09.011

SUMMARY

Working memory is a form of short-term memory that involves maintaining and updating task-relevant information toward goal-directed pursuits. Classical models posit persistent activity in prefrontal cortex (PFC) as a primary neural correlate, but emerging views suggest additional mechanisms may exist. We screened ~200 genetically diverse mice on a working memory task and identified a genetic locus on chromosome 5 that contributes to a substantial proportion (17%) of the phenotypic variance. Within the locus, we identified a gene encoding an orphan G-protein-coupled receptor, *Gpr12*, which is sufficient to drive substantial and bidirectional changes in working memory. Molecular, cellular, and imaging studies revealed that *Gpr12* enables high thalamus-PFC synchrony to support memory maintenance and choice accuracy. These findings identify an orphan receptor as a potent modifier of short-term memory and supplement classical PFC-based models with an emerging thalamus-centric framework for the mechanistic understanding of working memory.

INTRODUCTION

Humans use working memory pervasively from reading the newspaper to crossing a busy intersection. More precisely, working memory is (1) the ability to temporarily store task-relevant information from seconds to minutes in the absence of sensory input while (2) manipulating this information toward purposeful pursuits (Goldman-Rakic, 1995). This dual process of maintenance (e.g., remembering previous sentences in a newspaper) and manipulation (anticipating what may come next) requires high attentional and cognitive demand and has been linked to intellectual aptitude and higher-order executive functions (Conway et al., 2003; Baddeley and Hitch, 1974). Deficits in working memory are particularly prominent in learning disability, aging, attention deficit hyperactivity disorder (ADHD), Alzheimer's disease, and schizophrenia (Baddeley, 2003).

Early lesion studies established a fundamental role for prefrontal cortex (PFC) in working memory (Jacobsen, 1936). Subsequent neurophysiological studies in primates (Fuster and Alexander, 1971; Miller et al., 1993; Funahashi et al., 1993; Romo et al., 1999) and rodents (Fujisawa et al., 2008; Erlich et al., 2011; Harvey et al., 2012; Bolkan et al., 2017) identified a striking neural correlate for working memory—the persistent firing of cortical neurons when sensory information is being maintained during a delay period, prior to action selection. Such persistent firing, lasting seconds to minutes, has been enigmatic given that it far outlasts the millisecond-level operational time constant of individual neurons. Despite decades of study, we lack consensus on brain mechanisms that generate this persistent activity (Baddeley, 2012; Zylberberg and Strowbridge, 2017). Some models suggest cell-autonomous processes (Loewenstein et al., 2005; Egorov et al., 2002; Wang et al., 2011, Thuault et al., 2013), while others propose feedforward or recurrent activity in local (Brody et al., 2003; Lim and Goldman, 2013; Barak and Tsodyks, 2014) or long-range circuits (Guo et al., 2017; Bolkan et al., 2017). There is also growing appreciation for mechanisms beyond persistent activity, especially to account for multi-item storage and robustness to interference (Miller et al., 2018). Thus, more complete models are required.

In the past, unbiased genetic mapping approaches were foundational in revealing basic molecular mechanisms that can link neurophysiology and behavior (Dudai et al., 1976; Quinn et al., 1979; Bargiello et al., 1984; Nuzhdin et al., 1997; de Bono and Bargmann, 1998). Despite their power, these pioneering gene mapping approaches in invertebrates were limited by (1) mapping resolution (making the mapping of single genes laborious) and (2) an inability to assess higher-order cognitive processes such as selective attention and working memory. Taking inspiration from these approaches, and to address apparent limitations, we here performed quantitative trait loci (QTL) mapping in

Please cite this article in press as: Hsiao et al., A Thalamic Orphan Receptor Drives Variability in Short-Term Memory, Cell (2020), https://doi.org/10.1016/j.cell.2020.09.011

genetically diverse mice using the Diversity Outbred (DO) resource. Each DO mouse represents a unique mosaic of the parental strains and has a high degree of heterozygosity. Together they provide an ideal platform for high-resolution genetic mapping (Churchill et al., 2012). Accordingly, the DO (Carmody et al., 2015; Chick et al., 2016, Coffey et al., 2019, Saul et al., 2019) and other genetically diverse cohorts (Nicod et al., 2016; Parker et al., 2016) have been used in a series of studies that have elegantly associated genetic loci to a variety of traits. The emergence of this resource, together with concomitant advances in gene editing and circuit mapping technologies, offers a new opportunity for unbiased exploration of the molecular and neural circuit mechanisms of working memory.

Here, we phenotyped ~200 DO mice in a working memory task and identified a significant QTL on chromosome 5 (~4 Mb peak QTL, CI > 95%). Further examination of this locus, through gene-expression, loss of function, and behavioral studies, revealed a gene encoding an orphan G-protein-coupled receptor, *Gpr12*, that is required for, and can functionally promote, working memory. Subsequent molecular, cellular, and *in vivo* imaging studies together revealed that GPR12 is localized to the dendrites of thalamocortical neurons, facilitates activity-dependent calcium responses, and enables thalamocortical synchrony supporting behavioral performance. These results highlight a critical *Gpr12*-dependent thalamic contribution to working memory.

RESULTS

Identification of a QTL Linked to Working Memory

The power to detect QTL in mapping studies depends on the relative magnitude of statistical signal to noise, which is influenced by (1) the reliability and reproducibility of the quantitative trait values and (2) robust genetic contribution to the phenotypic variance. To evaluate these parameters, we performed pilot experiments of common cognitive and social rodent behaviors in the founder strains (n = 8/strain) that contributed to the DO population. In some assays, including behaviors with innate, learned, and cognitive components, we observed substantially greater phenotypic variation across strains than within strain, suggesting genetic contribution likely outweighs that of technical artifacts (Figure S1A). We proceeded to perform a large-scale study using the DO population (Figure 1A) to study working memory, and specifically spatial working memory, which is well characterized in rodents (Dudchenko 2004) and has a strong heritable component in humans (Knowles et al., 2014). We reasoned that 200 mice would provide sufficient power (60%–80%) to detect a QTL driven by a common allele that shifts the trait mean by 1 standard deviation at 95% confidence (Churchill et al., 2012).

To assess working memory, we chose to assay the mice in a spontaneous alternation test, in which mice prefer to explore a new arm of a T-maze on every visit. In order to perform the task significantly above chance (22%), mice must remember the sequence of previously explored arms (Lalonde, 2002). Although performance on the task can be confounded by effects of sensory, motor, and motivational processes (which we attempted to control for post hoc), we chose this task because it requires minimal intervention. In particular, it is not subject to the variabilities often introduced by training, learning, or food/water deprivation and therefore would provide a high-throughput behavioral screen.

After phenotyping 193 mice (STAR Methods), we first confirmed that their phenotypic variation greatly exceeded that of the commonly used C57BL/6J inbred strain (Figure 1B; Table S1). Using a Bayesian linear mixed model, we estimated heritability to 46.2% (95% CI: 22.2%–69.1%), which is consistent with an important contribution of genetics to the observed phenotypic variability. In this task, mice can perform poorly for reasons unrelated to short-term memory, such as sensory, motor, or motivational deficits, or on the contrary, can perform exceptionally well if they have stereotypy (e.g., continuously turning right). We therefore assessed and found no systematic correlation between task performance and measures of gross motor ability, exploratory drive, motivation, stereotypy, body physique, or gross sensory ability (Figures 1C–1F; Table S1).

All mice were subsequently genotyped using the GigaMUGA platform (114,184 loci were found to have variability in our cohort). Founder haplotype reconstructions were performed with a hidden Markov model approach using R/qtl2 (Broman et al., 2019), which showed robust allelic heterozygosity across the genome (Figure 1G). Approximately equal founder contributions were observed across the population (Figure S1B), suggesting minimal genetic drift and allelic loss. We performed QTL mapping (Figure S1C) for working memory performance in 182 DO mice (11 mice with latency to first arm entry >180 s were excluded from analysis). We identified a single QTL, *Smart1* (spontaneous T-maze alternation QTL 1), that is significant at a genome-wide p value of $\leq$0.01 on chromosome 5 (LOD score = 8.3, 95% CI: 143.2 Mb to 147.3 Mb) that explains 17% of the phenotypic variance (Figure S1D). *Smart1* was also detected using another mapping approach, miQTL (Figures 1H and 1I), which is designed to assess whether uncertainty in founder haplotype reconstruction is strongly influencing the result. We also noticed potential peaks on chromosome 13 and 15; however, they did not rise to our threshold of significance (Figure 1H). It is possible that future analyses with larger DO cohorts will offer sufficient power to detect more modest effects and thereby resolve these peaks. In this study, though, we chose to focus on the clearly significant signal at *Smart1*.

Smart1^{CAST} Is Associated with Increased Cognitive Performance

Next, we aimed to increase confidence that *Smart1* is indeed important for driving variance in working memory performance. To do so, we performed an allele effects analysis (STAR Methods) at this locus and found that the CAST/EiJ haplotype (henceforth referred to as *Smart1*^{CAST}) is associated with high performance while the C57BL/6J haplotype (henceforth referred to as *Smart1*^{B6}) is associated with poor performance (Figure 2A). A breakdown of the performance of individual mice by founder haplotype pairs (which we refer to as diplotype) at *Smart1* revealed that, strikingly, 80% of mice with *Smart1*^{CAST} performed above the mean of the DO cohort, whereas this was true of only 20% of mice with *Smart1*^{B6} (Figures 2B and 2C). Accordingly, mice with a *Smart1*$^{CAST/CAST}$ (F × F) exhibited the highest performance (alongside E × F mice), while mice with a *Smart1*$^{B6/B6}$ (B × B) exhibited the lowest performance (Figure S1E).

Please cite this article in press as: Hsiao et al., A Thalamic Orphan Receptor Drives Variability in Short-Term Memory, Cell (2020), https://doi.org/10.1016/j.cell.2020.09.011

CellPress

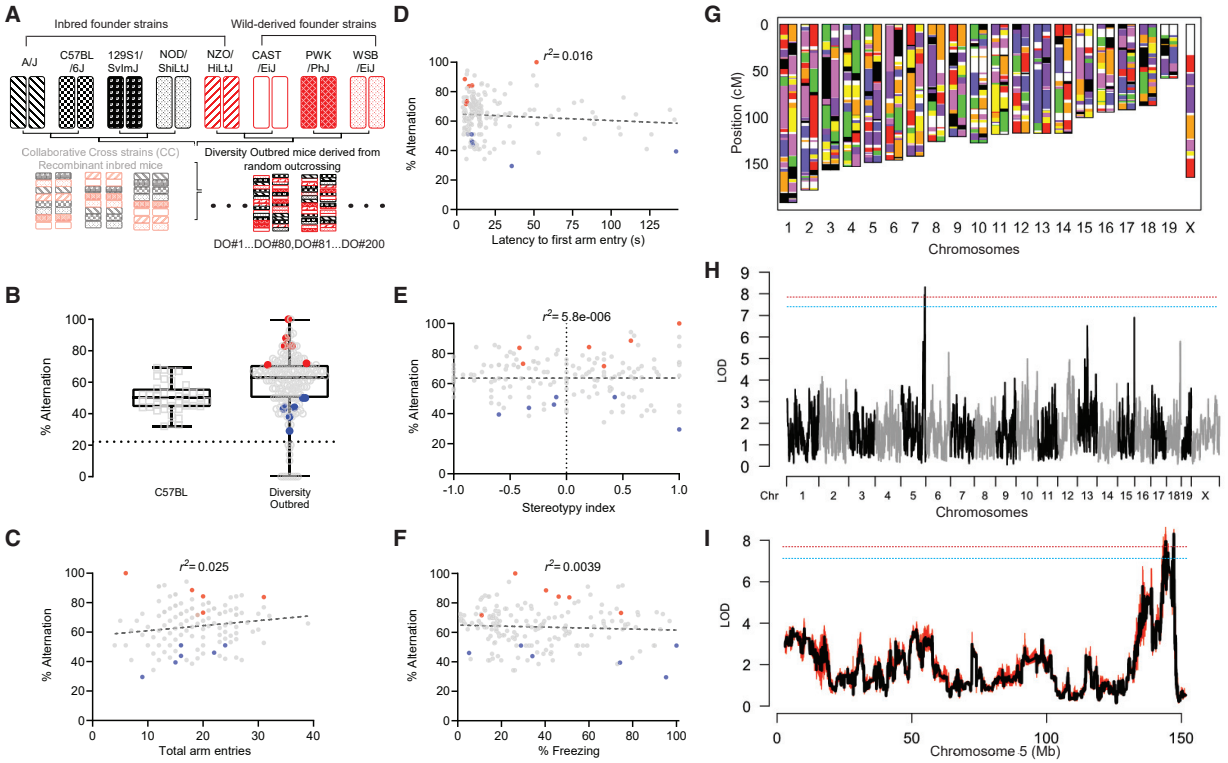

Figure 1. Identification of a Quantitative Trait Locus (QTL) Linked to Working Memory

(A) Outbreeding scheme to generate the DO and CC mice.

(B) Working memory performance of DO mice (n = 193) compared with C57BL/6J mice (n = 35) aggregated throughout the study. Mean, quartiles, minimum, and maximum are indicated. High- (red) and low- (blue) quartile-performing mice were selected for RNA-seq (in Figure 3).

(C–F) Correlations between spontaneous alternation performance and number of arm entries (C), latency to first arm entry (D), stereotypic movement (E), and contextual memory retrieval in fear conditioning (F). No significant Pearson's correlations. High- (red) and low- (blue) quartile performers from (B).

(G) Example haplotype reconstruction for one DO mouse demonstrating genetic mosaicism of parental lines and substantial allelic heterozygosity.

(H) QTL analysis (by miQTL) for spontaneous alternation. Significance thresholds after 1,000x permutations of genotype, blue: 90%, red: 95%.

(I) Mapping analyses performed using both R/qtl2 (black) and miQTL (red) revealing minimal fluctuation in LOD score across imputations (overlapping bands). See also Figure S1.

Furthermore, *Smart1*^{CAST} (F) when paired with any other founder haplotype was sufficient to improve performance to above average, while *Smart1*^{B6} (B) when paired with any other founder haplotype was sufficient to reduce performance to below average (Figure S1E). The only exception to the latter was mice with the B × F diplotype, which had below-average performance, suggestive of dominance of the *Smart1*^{B6} haplotype.

We then asked whether a genetically stable, multi-parent panel of recombinant inbred (RI) lines bearing either the CAST or C57 haplotype at *Smart1* would naturally segregate into high and low performers respectively. The Collaborative Cross (CC) mouse resource (Churchill et al., 2004), which share the same founders as the DO population but have been inbred to produce genetically reproducible strains, were used to validate our findings from the analysis of DO mice (Figure 2D). We analyzed the genotypes of existing CC lines and identified two lines (CC012 and CC046) that, while representing unique and independent mosaics of the founder genomes, possessed *Smart1*$^{CAST/CAST}$. We found that CC046 and CC012 mice outperformed mice bearing *Smart1*$^{B6/B6}$, CC004 and C57, respectively (Figure 2E), which was not due to differences in motor ability or motivation (Figures S1G and S1H). We further tested these mice in another working memory task, delayed non-match to place (DNMP) (Dias and Aggleton, 2000), in which mice first collect reward in one arm, then after a brief delay (10 s), learn that the subsequent reward will be in the opposite arm. After learning, progressive increases in delay period length reflect increases in working memory demand. Although all mice learned the task at the same rate (Figure 2F), CC012 (*Smart1*$^{CAST/CAST}$) performed significantly better than C57 when the delay period was increased to 20 s or 30 s (Figure 2G). These data indicate that genetic variation at *Smart1* is sufficient to drive variation in working memory performance and that *Smart1*^{CAST} is associated with improved working memory.

Smart1 Encodes an Orphan GPCR, Driving Variability in Working Memory

We next aimed to determine which gene or variant within the locus is causally involved in driving variation in working memory

Please cite this article in press as: Hsiao et al., A Thalamic Orphan Receptor Drives Variability in Short-Term Memory, Cell (2020), https://doi.org/10.1016/j.cell.2020.09.011

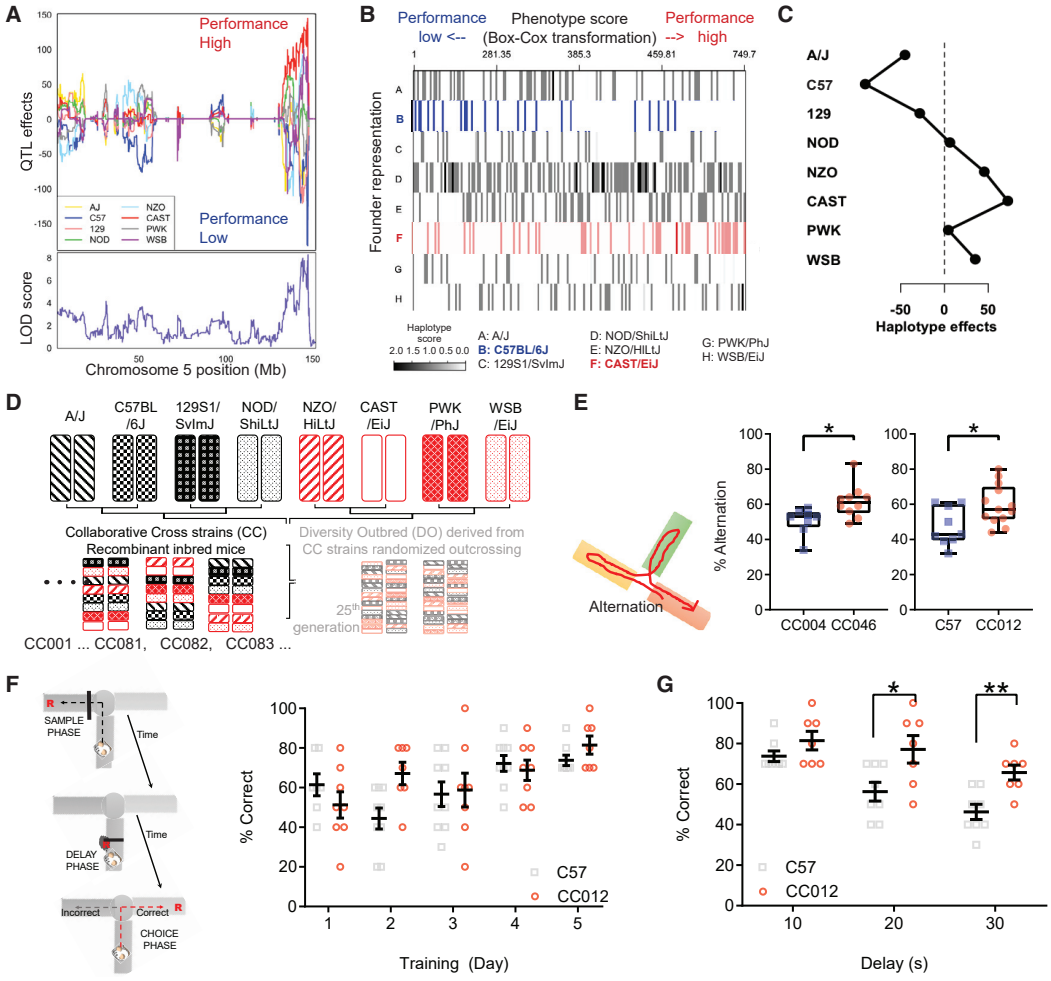

Figure 2. *Smart1* Locus Confers Performance Variation in Working Memory

(A) Effect of each founder allele on spontaneous alternation performance along chromosome 5 (Chr 5) (x axis), as measured by the founder coefficients from the linkage model (y axis). Coefficients diverge substantially at the peak QTL. Logarithm of odds (LOD) score at each chromosomal position shown.

(B) Heatmap where each dashed line depicts an individual mouse, with row indicating founder haplotype allele contribution at Chr 5 locus, and column indicating boxcox transformed performance score on spontaneous alternation.

(C) Similar to (B) but displaying haplotype representation at the Chr 5 locus and corresponding *Z* scored phenotypes, quantified as mean ± SEM.

(D) Overview of the breeding scheme to create CC mouse strains.

(E) CC mice bearing CAST diplotype at *Smart1* locus (CC046 and CC012) were compared respectively with mice bearing B6 diplotype at the same locus (CC004 and C57BL/6J) in spontaneous alternation. $p < 0.05$, unpaired t test with Welch's correction.

(F) Schematic illustration of DNMP. Performance (% correct) shown for CC012 (n = 7) versus C57 (n = 8) during training (10 trials/day). No significant differences, two-way ANOVA with repeated measures.

(G) % correct by CC012 (n = 7 mice) and C57 mice (n = 8) for variable delays (10 trials/day). Data are mean ± SEM. *p(20 s) = 0.027, **p(30 s) = 0.002, two-way ANOVA with repeated measures followed by Bonferroni's test.

See also Figure S1.

performance. The preponderance of SNPs in non-coding regions (Figures S2A–S2C) suggested potential gene regulatory, and therefore gene expression, differences between high and low performers. We isolated brain regions with known or potential relevance for working memory including PFC, hippocampus (HPC), association thalamus, and ventral tegmental area (VTA), from high- (n = 3, $Smart1^{CAST}$) and low- (n = 3, $Smart1^{B6}$) performing DO mice. After verifying that the dissections were well-targeted (Figures S2D and S2E), we performed RNA sequencing (RNA-seq) from those four brain regions and from six mice (STAR Methods).

High and low performers were stratified in all regions, including the PFC, which is the region most tied to working memory function (Figure 3A). However, of the four brain regions assessed, the

Please cite this article in press as: Hsiao et al., A Thalamic Orphan Receptor Drives Variability in Short-Term Memory, Cell (2020), https://doi.org/10.1016/j.cell.2020.09.011

CellPress

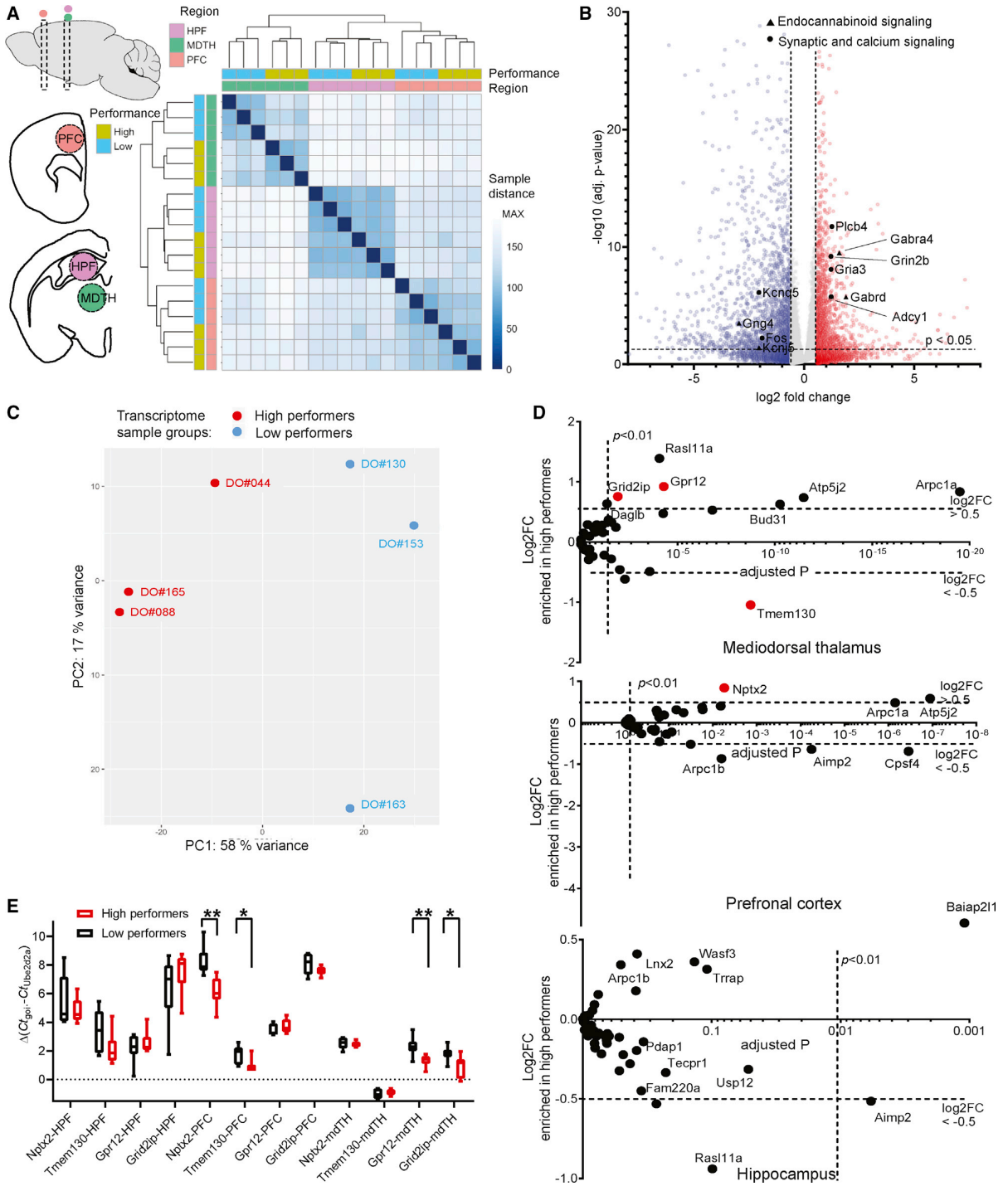

Figure 3. Distinct Patterns of Thalamic Gene Expression Distinguish Performance

(A) Left: schematic of dissected brain regions for RNA-seq. Right: heatmap of hierarchical clustering by Euclidean distance among gene expression profiles in DO high (n = 3) and low performers (n = 3) as highlighted in Figure 1B and from three brain regions per mouse: PFC, mediodorsal thalamus, and HPC. Clustering is visible by brain region and performance.

(legend continued on next page)

Please cite this article in press as: Hsiao et al., A Thalamic Orphan Receptor Drives Variability in Short-Term Memory, Cell (2020), https://doi.org/10.1016/j.cell.2020.09.011

mediodorsal thalamus exhibited the strongest clustering by performance, revealing a more global reprogramming of the transcriptome differentiating high and low performers (Figure 3A; Euclidean distance in mediodorsal thalamus = 30, HPC = 8, PFC = 13; VTA not shown). Enrichr analysis of genes contributing to the first principal component revealed three prominent signaling pathways: (1) synaptic signaling, (2) endocannabinoid signaling, and (3) calcium signaling (Figures 3B and 3C; PC1: 58% variance). Of the genes at the locus, one gene in PFC (*Nptx2*) and three genes in mediodorsal thalamus (*Tmem130*, *Gpr12*, *Grid2ip*) passed the criteria of (1) robust expression ($\geq$1,000 reads) (Figure 3D) and (2) significant expression fold difference between high and low performers (log2FC > 0.5 and adjusted $p < 0.01$) (Figures 3D and 3E).

We next determined which, if any, of these four genes, could causally drive changes in working memory performance. We developed and validated AAV-based RNA interference (RNAi) constructs to target *Tmem130*, *Nptx2*, and *Gpr12*, as well as an AAV-hSyn-driven overexpression for *Grid2ip* (the injection of RNAi to *Grid2ip* resulted in death for the majority of the cohort) (Figures S3A–S3C), and bilaterally injected into the appropriate (PFC or mediodorsal thalamus) brain regions for behavioral testing (Figure 4A). Of note, we chose to target *Tmem130* knockdown in thalamus (rather than PFC) because of the significantly greater expression levels in thalamus, together with the significant differential expression in thalamus by RNA-seq (Figure S2F). Since previous reports had linked the synaptogenic immediate early gene *Nptx2* (Xiao et al., 2017) and the glutamate receptor-interacting protein *Grid2ip* (Raghavan et al., 2018) to Alzheimer's, we expected their manipulation may contribute most to changes in working memory. Instead, we found, in blinded studies, that manipulation of an orphan GPCR, *Gpr12*, in mediodorsal thalamus significantly and bidirectionally regulated working memory (Figure 4A). *Gpr12* knockdown in mediodorsal thalamus of high-performing mice (CC012, $Smart1^{CAST/CAST}$) significantly reduced spontaneous alternation performance ($p < 0.001$, unpaired t test with Welch's correction), while overexpression in mediodorsal thalamus of low-performing (C57, $Smart1^{B6/B6}$) mice significantly improved mean performance (Figure 4A; $p < 0.01$, one-way ANOVA). Perturbations in the expression levels of *Nptx2*, *Grid2ip*, or *Tmem130* had no significant effect (Figure 4A).

The effects of *Gpr12* were more dramatic when testing mice on another working memory task, DNMP, which involves delay-dependent representation of stimuli and is sensitive to temporal interference. Blinded testing and analyses of two independent cohorts revealed that *Gpr12* knockdown in mediodorsal thalamus of high-performing CC012 mice significantly reduced delay-dependent working memory performance, shifting mean performance from 85% accuracy to 62% accuracy at the 30 s delay when compared with CC012 mice expressing scrambled RNAi controls (Figure 4B). Perhaps more strikingly, *Gpr12* overexpression in the mediodorsal thalamus of low-performing C57 mice was sufficient to increase working memory performance, significantly improving mean performance at the 20 s delay and more dramatically at the 30 s delay from 58% to 80% ($p < 0.001$, two-way ANOVA with repeated measures) when compared with C57s expressing mCherry control virus (Figure 4C). Importantly, no significant differences were observed during training (Figures 4B and 4C), and these effects were not observed in hippocampus (Figure 4D, S3D, and S3E). Furthermore, the effects of *Gpr12* were specific to working memory, as we saw no change in a test of spatial long-term memory (Figure 4E) and no apparent change in basic motor or motivational measures (Figure S3F). Post hoc histology and quantitative western blot confirmed that the expression constructs were expressing in the relevant brain regions (Figures S4A–S4C) and resulted in physiologically relevant ~1- to 2.5-fold increase in protein levels during overexpression and ~60% reduction during knockdown (Figure S4D). The *in vivo* knockdown of *Nptx2* and *Tmem130* was less efficient; therefore, we do not rule out the possibility that these genes or other genes at the *Smart1* locus that were not explicitly tested may have contributions to working memory. However, we do conclude with confidence that *Gpr12* expression in thalamus has strong, causal, and bidirectional contributions to working memory performance.

Gpr12 Facilitates Activity-Dependent Calcium Responses

Gpr12 is a Class A GPCR that is conserved in mammals including humans (Song et al., 1995). It belongs to a family of GPCRs that have no known ligand but are most closely related to lypophospholipid and cannabinoid receptor families (up to 40% homology) and less but significant homology with adenoreceptor and melanocortin receptor families. Accordingly, proposed native ligands include Tyrosol, SPC, and Nesfatin (all at nM affinity), while potential inverse agonists include cannabidiol (CBD) and pyrimidine analogs (weak affinities) (Morales et al., 2018). To understand further how *Gpr12* may contribute to working memory performance, we asked (1) where is it localized?, (2) what downstream signal transduction is it coupled to in those neurons?, and (3) how do these properties impact its cellular and circuit-level functions?

We obtained a commercially available antibody for GPR12, and validated it using *Gpr12* knockout HT22 cell lines (Figures S4I and S4J) and mouse brain tissue (Figures S4C and S4D).

(B) Volcano plots showing the significance and p value distribution after differential gene expression analysis in mediodorsal thalamus using DESeq2. n = 6, biologically independent samples. Black dots highlight calcium channels with expression in thalamus.
(C) Principal component analysis of performance-divided mediodorsal thalamus gene expression in two distinct groups (red, high performers; blue, low performers).
(D) Volcano plots displaying differential expression of all genes within *Smart1* (black dots) between high and low performers. Dashed vertical lines indicate significance threshold (adjusted $p < 0.01$) and dashed horizontal lines indicate threshold for differential expression (log2FC > 0.5 or < −0.5). Red dots indicate genes that cross significance and differential expression thresholds and have a DESeq2-normalized read-count >1000.
(E) Differential expression of four chosen genes (red dots in D) by qPCR (n = 6 ea.). *$p < 0.05$, **$p < 0.01$, by paired t test with Welch's correction.
See also Figure S2.

Please cite this article in press as: Hsiao et al., A Thalamic Orphan Receptor Drives Variability in Short-Term Memory, Cell (2020), https://doi.org/10.1016/j.cell.2020.09.011

CellPress

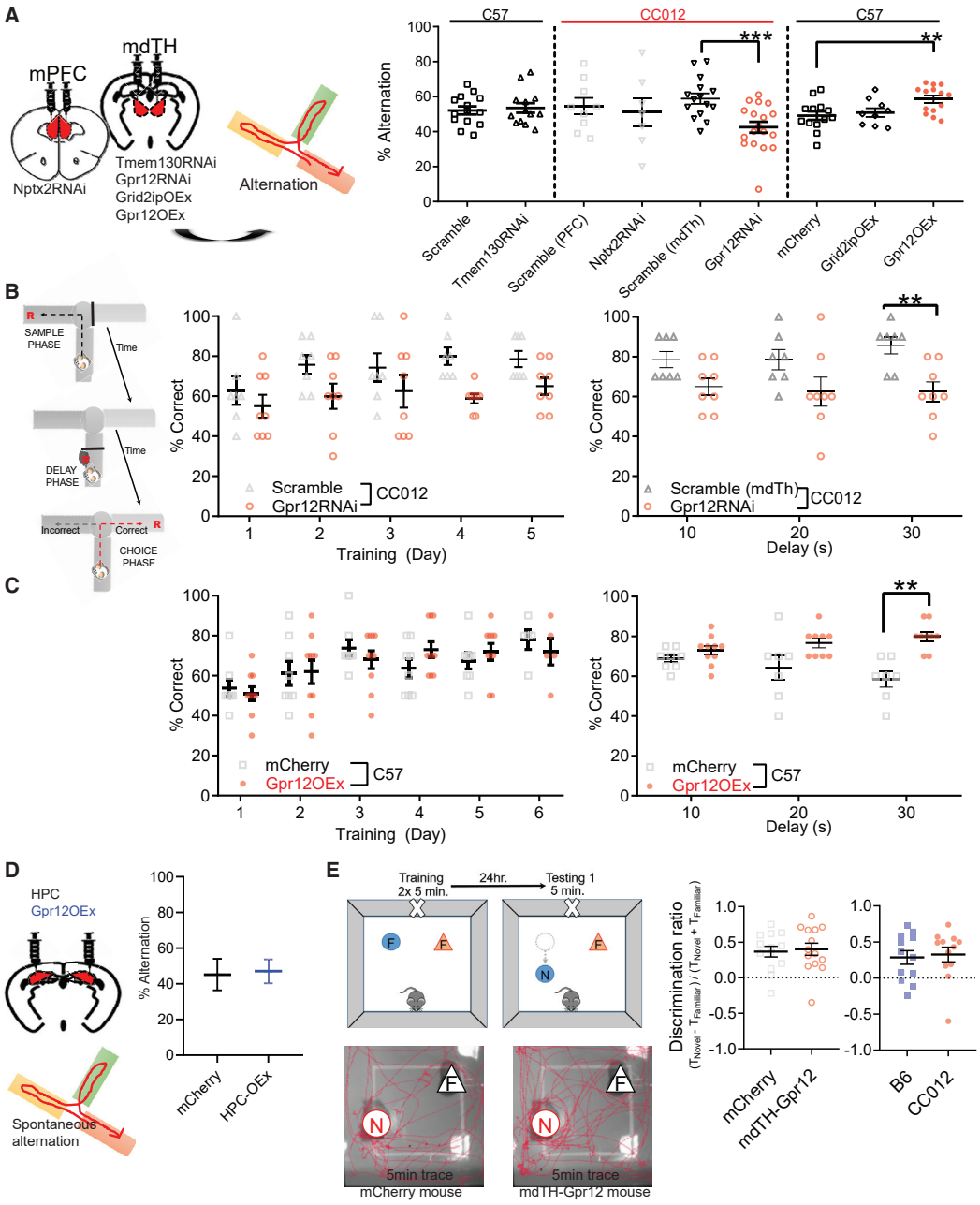

Figure 4. Thalamic Orphan Receptor *Gpr12* Promotes Working Memory

(A) Left: schematic of AAV used and brain regions tested. Right: effects on behavior in spontaneous alternation. Initially n = 10 per group, but some groups diminished because of animal death or absence of viral targeting. The Gpr12 group is a mix of two independent cohorts where each cohort achieved significance independently. Data are mean ± SEM. **p < 0.01 by one-way ANOVA, ***p < 0.001, by unpaired t test with Welch's correction.

(B) Left: % correct during training (10 trials/day) in CC012 mice with knockdown (n = 8) or scrambled control (n = 7) in thalamus. No significant differences by two-way ANOVA with repeated measures. Right: % correct during testing at variable delays (10 trials/day). *p < 0.05, **p < 0.01, two-way ANOVA with repeated measures followed by Bonferroni's test.

(C) Left: % correct during training (10 trials/day) in C57 mice with overexpression of *Gpr12* in thalamus (n = 10 grouped over two cohorts) or mCherry alone (n = 8 grouped over two cohorts). Right: half mice from both cohorts received 6 days of training. % correct during testing at variable delays (10 trials/day). Data are mean ± SEM. *p(20 s) = 0.015, ***p(30 s) < 0.001, two-way ANOVA with repeated measures followed by Bonferroni's test.

(D) AAV-based overexpression of *Gpr12* in HPC showed no significant differences. n = 11. Data are mean ± SEM p = 0.8724 by t test.

(legend continued on next page)

Please cite this article in press as: Hsiao et al., A Thalamic Orphan Receptor Drives Variability in Short-Term Memory, Cell (2020), https://doi.org/10.1016/j.cell.2020.09.011

We then performed immunohistochemistry for GPR12 and found prominent expression in thalamus (primarily mediodorsal thalamus), hippocampus (primarily the CA2 region), and several cortical regions (primarily layers 2/3 and 5) (Figure 5A). These expression distributions were corroborated by follow-up *in situ* hybridization (ISH) experiments directed toward the mature *Gpr12* messenger RNA (Figure 5B), as well as with publicly available single-cell sequencing data (Saunders et al., 2018). To determine whether *Gpr12* was expressed in a significant fraction of thalamocortical neurons, we retrogradely labeled neurons from layer 2/3 of medial prefrontal cortex (mPFC) and overlaid *Gpr12* expression by ISH. We found that approximately half of thalamocortical neurons contain *Gpr12* (Figures 5B and 5C), which may be an underestimate given ~100% specificity but ~75% sensitivity in GFP control ISH experiments (Figures 5B and S4E). Higher-resolution imaging of GPR12 revealed localization to the somato-dendritic compartment with lack of expression in axon terminals in PFC (Figure S4C). These expression and localization studies suggested that *Gpr12* may have functions in thalamus that gate or promote neural activity interactions with PFC.

To better understand cellular functions of *Gpr12*, we aimed to determine how *Gpr12* couples to downstream signaling pathways. GPCRs have been implicated in working memory (Dash et al., 2007; Arnsten and Jin, 2014) and tend to fall into three broad categories for downstream coupling: Gs (increased Ca^{2+} and cAMP signaling), Gq (PLC/Dag/IP3 pathway), and Gi/o (decreased cAMP signaling). To differentiate among these possibilities, we began by manipulating *Gpr12* in neuronal cell lines and assaying for resulting changes in calcium activity. Although no well-characterized high-affinity ligands currently exist for *Gpr12*, we reasoned that since *Gpr12* has constitutive receptor activity (Uhlenbrock et al., 2002), manipulation of expression level could serve as a proxy for activity levels. Upon transiently overexpressing *Gpr12* in neuronally differentiated HT-22 cells (Figure 5D; STAR Methods), we observed appreciable increases in the probability and magnitude of glutamate-induced calcium events compared with mCherry-expressing controls (Figure 5E). On the other hand, CRISPR-mediated *Gpr12* knockout (Figures S4F–S4J) led to significant and prominent (almost 50%) reductions in the average glutamate-induced calcium response (Figures 5F and 5G). These experiments demonstrate that *Gpr12* couples to signaling pathways that eventually lead to increases in activity-dependent calcium responses (Figure 5H).

To understand further how *Gpr12* mediates increases in activity-induced calcium levels, we challenged HT22-derived neuronal cells with selective antagonists to known thalamic expressing voltage-gated calcium channels (VGCCs) (targeting T-type, L-type, and Hyperpolarization-activated cyclic nucleotide-gated (HCN) channels; Figure S5A), in both wild-type and *Gpr12* knockout cell lines, and under spontaneous as well as glutamate-induced conditions (Figure 5F). We found that the glutamate-induced calcium responses in *Gpr12*-expressing groups (wild-type) were most susceptible to the L-type VGCC blockade, marked by significant reduction (~60%), whereas in *Gpr12* null groups (knockout), no reductions were observed (Figures 5I and 5J). On the contrary, both T-type and HCN blockers did not significantly discriminate between *Gpr12* positive or null groups, suggesting they act on mechanisms independent of *Gpr12* (Figures 5I and 5J). Accordingly, we also noted that of these VGCCs, only the L-type Cav1.2 channel was significantly upregulated in high-performing DO mice (Figure S5A). In summary, these experiments demonstrate that *Gpr12* is localized to the somato-dendritic compartment of a subset of thalamocortical projecting neurons, has preferential coupling to L-type channels, and promotes the fidelity and magnitude of excitatory transmission.

Smart1^{CAST} Performance Accuracy Associated with Increased *Gpr12* and Elevated Thalamocortical Synchrony during Memory Maintenance

Does *Gpr12* have similar functions *in vivo*? Does it couple to increases in activity-dependent calcium responses, and more importantly, how does that affect dialog with other relevant brain circuits, especially during working memory? To address these questions, we moved to an *in vivo* preparation where we used fiber photometry (Cui et al., 2013; Kim et al., 2016) to record bulk neural activity from PFC, mediodorsal thalamus, and HPC from low- (C57) and high- (CC012) performing mice during the DNMP task (Figures 6A–6C). Of note, CC012 lines (*Smart1*$^{CAST/CAST}$) have ~2.5-fold higher mediodorsal thalamic expression of *Gpr12* than low-performing C57s (*Smart1*$^{B6/B6}$) (Figure 6D). We injected AAV9-GCaMP6f in PFC, mediodorsal thalamus, and HPC and implanted optical fibers above each region to record neural activity. Sufficient expression and accurate implantation of the injection site were confirmed by histology (Figures S5B and S5C). Neural activity recordings from multiple regions of a given animal were frame projected onto a camera sensor, and custom MATLAB scripts (STAR Methods) were used to extract time-series data, regress out motion-related artifacts, and align to behavioral data (one example alignment shown in Figure 6C; additional raw traces in Figures S6A and S6B).

While in the home cage, no significant differences between C57 and CC012 strains in average activity of any of the brain regions or in correlated patterns of activity between any two brain regions were observed (Figure 6E). However, during the task, we found that CC012 mice displayed significantly enhanced activity correlations between mediodorsal thalamus and PFC during several phases of the task (Figure 6F; all trials shown in Figure S6E), which were reduced or absent in thalamus-HPC or PFC-HPC interactions and which was not due to differences in animal speed (Figure S6C), motion artifacts (Figure S6D), or accruing noise correlations in the GCaMP signal (Figure 6F; i.e., chance Pearson for delay period = 0.1 ± 0.2, 1,000x circular permutation). We also note that neurites are unlikely to

(E) Left top: diagram of Object Place Memory task. Left bottom: example traces from one mouse in each cohort in the presence of novel (N) and familiar (F) objects. Right: no significant differences in long-term spatial memory between mCherry (7 mice, 13 trials) and mdTH-Gpr12 (7 mice, 14 trials), p = 0.7749 Unpaired t test; neither between C57(B6) (6 mice, 12 trials) and CC012 (6 mice, 12 trials), p = 0.7705 Unpaired t test.
See also Figures S3 and S4.

Please cite this article in press as: Hsiao et al., A Thalamic Orphan Receptor Drives Variability in Short-Term Memory, Cell (2020), https://doi.org/10.1016/j.cell.2020.09.011

CellPress

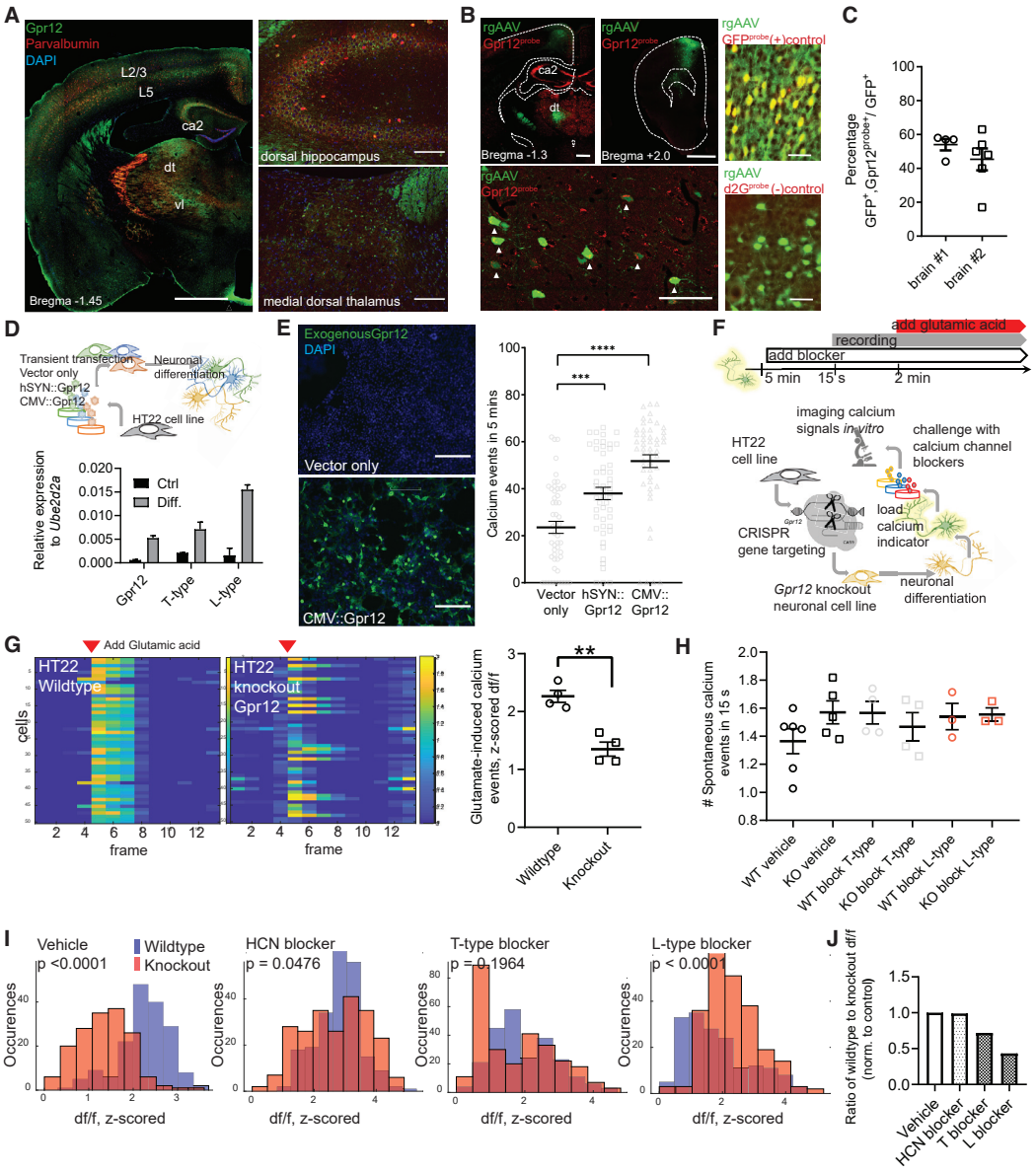

Figure 5. *Gpr12* Expresses in Thalamocortical Neurons and Facilitates Calcium Responses

(A) Immuo-histochemistry with anti-Gpr12 (green) and anti-parvalbumin (red) antibodies showing endogenous Gpr12 distribution. Images were collected with ×10 objective and tiled together to generate high-resolution images of brain sections. The acquired images were processed using the NIS-Elements (Nikon). dt, dorsal thalamus; vt, ventral thalamus; ca2, hippocampus; L2/3 and 5, Cortex. Left scale: 1 mm; Right scale: 500 μm.

(B) *In situ* hybridization of Gpr12 mRNA (left), control probes for GFP mRNA (right top) and d2GPF mRNA (right bottom) in thalamus (red), and overlay with retrograde virus from mPFC (rgAAV-GFP) (green). Arrowheads point to significant overlay. Images were collected with ×10 or ×40 objectives and tiled together to generate high-resolution images of brain sections. The acquired images were processed using the Zen (Zeiss). Scale bars left: 500 μm (top), 100 μm (bottom); right: 50 μm.

(C) Fraction of GFP+ neurons (green) that are Gpr12+ (red). n = 4 slices in first experiment, n = 5 slices in second experiment. Data are mean ± SEM.

(D) Top: schematic of neural differentiation of HT-22. Bottom: increased expression of neuronal genes after differentiation. Data are mean ± S.E.M, n = 4 experiments.

(E) Left: Vector only control transfection and *Gpr12* overexpression using a cytomegalovirus (CMV) promoter in HT22 cells; scale bar: 250 μm. Right: glutamate-induced calcium events during 2 min bath application of glutamic acid (10 mM) in cells with vector only, hSyn-driven *Gpr12*, and CMV-driven *Gpr12*. Data are mean ± SD, n = 50–80 cells. ***p < 0.001, ****p < 0.0001, t test.

(F) Schematic and timeline of experiment performed.

(legend continued on next page)

Please cite this article in press as: Hsiao et al., A Thalamic Orphan Receptor Drives Variability in Short-Term Memory, Cell (2020), https://doi.org/10.1016/j.cell.2020.09.011

contribute to the observed mediodorsal thalamus-PFC correlations because (1) we intentionally implanted these cannulas contra-laterally (the recurrent projections are primarily ipsilateral), and (2) the increased mediodorsal thalamus-PFC correlations was specific to CC012 mice, despite the fact that both strains had similar mean calcium activity in PFC and thalamus during behavior (Figure 6E, upper), and therefore similar contributions to activity in projection terminals.

We then asked whether the observed circuit level effects between CC012 versus C57 were attributable primarily to differences at the *Smart1* locus and to differences in expression of *Gpr12*. We therefore recorded bulk GCaMP6f-based neural activity in mice with overexpression of *Gpr12* in mediodorsal thalamus (Gpr12) or RFP control vector (RFP). Sufficient expression and accurate implantation of the injection site were confirmed by histology (Figures S5D and S5E) and resulted in physiologically relevant ~2-fold increase in *Gpr12* transcript levels, comparable to ~3-fold increase observed in CC012 mice (Figure S5F). As expected, Gpr12 mice had significantly higher delay-dependent working memory performance than the RFP control cohort (Figure 6B). In assessing brain activity, we found that Gpr12 mice displayed enhanced thalamocortical activity correlations during the encoding and memory maintenance phases of the task but not during start, choice, or reward (Figure 6G; all trials in Figure S6F; no significant correlation with animal speed; Figure S6G). Therefore, while the neural activity patterns in Gpr12 mice largely confirmed the findings from CC012 mice, the results suggest that *Gpr12* has a specific role in targeting only thalamocortical synchrony and only for particular phases of the task (Figure S6E compared with Figure S6F). Finally, not only were thalamocortical synchrony indicative of overall performance but, importantly, were predictive of accuracy on a trial-by-trial basis (Figure 6H). These results demonstrate that *Gpr12* is critical, and indeed sufficient, for enhancing thalamocortical synchrony during working memory.

Lastly, we searched for additional features of *Gpr12*-dependent neural activity patterns, beyond thalamocortical synchrony, that contributed to working memory choice accuracy. We observed that the magnitude of PFC activity succeeding the delay period, but just prior to the choice point (C'D), was highly predictive of upcoming decision, i.e., higher PFC activity was significantly more likely to lead to a correct choice (Figure 6I; $p < 0.001$, Tukey's Multiple Comparisons). Furthermore, only PFC activity at the choice point was informative, since neither the PFC activity during other periods of the task nor the mediodorsal thalamus and HPC signals at the choice point were predictive of trial accuracy (Figure S6H). These results suggest a model in which mediodorsal thalamus-PFC synchrony during the delay period may enable the memory maintenance aspects of working memory, while transfer of control to PFC during the choice period may enable the executive component of working memory required for goal directed actions. These results demonstrate a critical Gpr12-dependent thalamic contribution to working memory and support more broadly the importance of thalamic contributions to higher-order cognitive processing (Baddeley, 2012; Schmitt et al., 2017).

DISCUSSION

Using an unbiased genetic mapping approach in outbred mice, we identified a genomic locus, *Smart1*, that is critical for explaining variation in a higher order cognitive process—working memory. Further characterization of this locus revealed an orphan GPCR, *Gpr12*, that is not only required for working memory but, more importantly, its overexpression in thalamus is sufficient to reproduce the $Smart1^{CAST}$ -associated increased performance in delay-dependent and -independent measures of working memory (SA and DNMP). Interestingly, *Gpr12* is conserved only in mammals, including humans (consistent with a role in higher-order cognition), and human genome-wide association studies have reported intergenic *GPR12* variants associated with cognitive performance (Lee et al., 2018) as well as with treatment response in schizophrenia (Drago and Kure Fischer, 2018), a condition with significant working memory deficits.

The transcriptome-wide reprogramming of mediodorsal thalamus between high- and low-performing mice, the mediodorsal thalamus-specific behavioral effects of $Smart1^{CAST}$, and the functional contributions of *Gpr12* all point toward a predominant role for thalamus in the working memory process. While pioneering studies have highlighted the importance of the PFC, there were also early hints in primate studies of the involvement of other brain structures (Constantinidis and Procyk, 2004). More recent studies have begun to articulate these complementary roles of other brain circuits (Parnaudeau et al., 2013; Harvey et al., 2012; Akrami et al., 2018; Kupferschmidt and Gordon, 2018), and in this regard, emerging studies have revisited the involvement of the thalamus (Kupferschmidt and Gordon, 2018; Bolkan et al., 2017). Here, we join these studies in emphasizing that an entirely unbiased approach highlighted critical mediodorsal thalamus contributions and extend these studies in two important ways: (1) we provide an entry point (*Gpr12*-driven signaling) toward tangible insights into the molecular mechanisms mediating long range synchrony during working memory, and (2) we provide insights into the functional role of thalamus through simultaneous neural activity recordings from PFC, mediodorsal thalamus, and HPC during working memory. We found that mice overexpressing thalamic Gpr12 display striking thalamocortical synchrony during the encoding

(G) Heatmap of *Z* scored calcium events before and after bath application of 10 mM glutamic acid (red triangle), in wild-type and *Gpr12* knockout cells. Data are mean ± SEM, n = 4 experiments, unpaired t test, **p = 0.0012.
(H) Quantifications of spontaneous calcium events in a 15 s window after 5 min bath application of T-type or L-type VGCC block (n = 4) or vehicle control (DMSO, 1000x dilution, n = 5). Data are mean ± SEM. No significant differences, unpaired t test.
(I) Frequency of glutamic-acid-induced calcium responses during bath application of blockers or vehicle in neurons derived from wild-type or *Gpr12* knockout HT22.
(J) Quantification of each VGCC blockade in (I). *Gpr12*-dependent effect is represented by ($WT^{blocker}$ / $WT^{vehicle}$) over ($KO^{blocker}$ / $KO^{vehicle}$).
See also Figure S4.

Please cite this article in press as: Hsiao et al., A Thalamic Orphan Receptor Drives Variability in Short-Term Memory, Cell (2020), https://doi.org/10.1016/j.cell.2020.09.011

CellPress

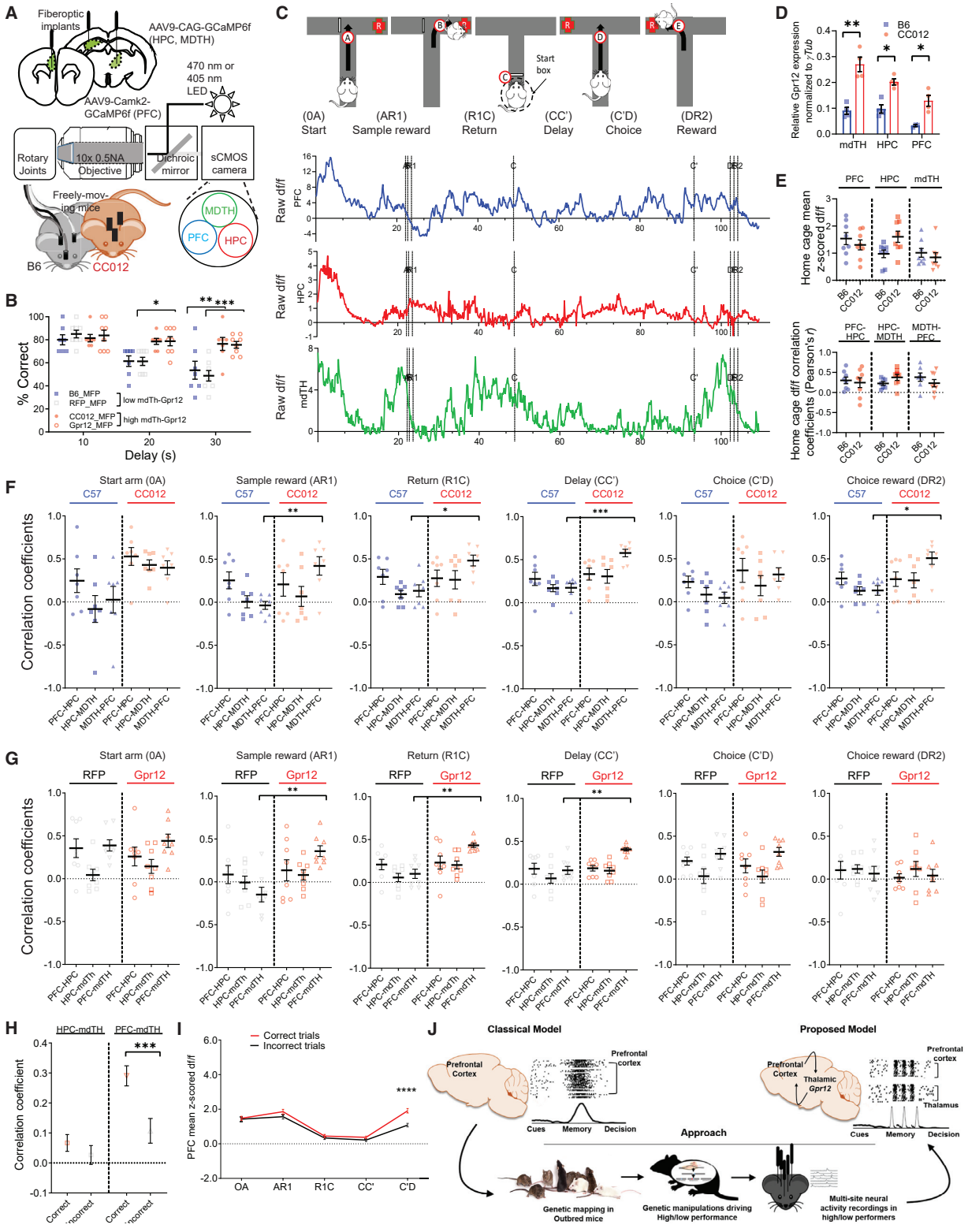

(legend on next page)

Please cite this article in press as: Hsiao et al., A Thalamic Orphan Receptor Drives Variability in Short-Term Memory, Cell (2020), https://doi.org/10.1016/j.cell.2020.09.011

and memory maintenance phases of the task (but not between thalamus-HPC or PFC-HPC) that led to increased choice accuracy. The underlying source of this synchrony, however, is still unclear. Subsequent to the delay period, the synchrony abruptly disappeared but high PFC activity was maintained, and preferentially on correct trials. These results suggest that thalamus may serve not only to enhance short-term memory during the delay period but also for handoff to PFC for subsequent executive control and choice. Given recent reports of the contributions of mediodorsal thalamus in sensory gating and attention (Schmitt et al., 2017), it is possible that *Gpr12* functions to enhance attention during working memory, but because the impact of *Gpr12* progressively increased during successively longer delay periods (from 10 s up to 45 s), a more specific role in the maintenance of working memory is likely. Furthermore, a previous study reported on the importance of long-range synchrony between motor thalamus and motor cortex in sustaining motor planning (Guo et al., 2017), which, together with recent reports (Bolkan et al., 2017; Schmitt et al., 2017) and our work, suggests common thalamocortical motifs in sustaining neural representations across sensory, cognitive, and motor domains.

Future studies investigating *Gpr12* cellular and circuit mechanisms will further clarify existing models of working memory (Miller et al., 2018), where our current data favor persistent activity interleaved with periods of short-term plasticity (Figure 6J). It will also be important to explore whether *Gpr12* contributes to non-spatial and more general forms of working memory and whether other genetic loci may complement *Gpr12* functions during working memory. Finally, manipulations of mediodorsal thalamus during neural activity recordings of related circuits will add to our understanding of long-range synchrony (Katz and Shatz, 1996; Buzsáki et al., 2004; Harris and Gordon., 2015) and the dynamics of a broader neuroanatomically distributed network that shape this higher-order cognitive process (Kupferschmidt and Gordon, 2018). Notably, this study offers proof of principle that the DO population can be leveraged to identify QTLs with narrow intervals and large effect sizes that can reveal critical insights into cognitive processes. This may be a generalizable approach toward the use of rodent models to dissect discrete brain functions often amalgamated in neuropsychiatric disease (Tarantino and Bucan, 2000; Howe et al., 2018) and a powerful complement to human disease association studies.

STAR★METHODS

Detailed methods are provided in the online version of this paper and include the following:

- KEY RESOURCES TABLE
- RESOURCE AVAILABILITY
  - Lead Contact
  - Materials Availability
  - Data and Code Availability
- EXPERIMENTAL MODEL AND SUBJECT DETAILS
  - Mice
- METHOD DETAILS
  - QTL mapping in Diversity Outbred Mice
  - Animal Behaviors
  - Animal Surgical Procedures
  - RNA Expression Analysis
  - siRNA Experiments *In Vitro* & *In Vivo*
  - *In Vitro* Calcium Imaging
  - *In Vivo* Multi Site Photometry Recordings
- QUANTIFICATION AND STATISTICAL ANALYSIS
  - Behavior Statistical reporting
  - Gene Expression Statistics
  - Multi-Fiber Photometry Data Processing
  - Multi-Fiber Photometry Data Analysis

SUPPLEMENTAL INFORMATION

Supplemental Information can be found online at https://doi.org/10.1016/j.cell.2020.09.011.

Figure 6. *Smart1*^{CAST} Display High Thalamocortical Synchrony during Memory Maintenance Predictive of Performance

(A) Schematic of three-region fiber photometry. Top: coronal slices depicting fiber placements and corresponding viral constructs targeted to each region. Bottom: simultaneous 470 nm and 405 nm recordings of each region in C57 or CC012 strains.

(B) DNMP performance from two independent experiments: CC012 v B6, n = 7 ea., **p(30 s) = 0.008; Gpr12 v RFP, n = 8 ea., ***p(30 s) < 0.001, two-way ANOVA with repeated measures followed by Bonferroni's test.

(C) Example GCaMP6f traces from three brain regions aligned to one trial of DNMP.

(D) Endogenous *Gpr12* transcript levels in mdTH, HPC, PFC by qPCR, normalized to γTub and shown as mean ± SEM, *p < 0.05, **p < 0.005, t test.

(E) Top: average activity (area under *Z* scored responses) in home cage (CC012 versus C57, n = 8 ea., 1 min recording). Bottom: pairwise Pearson's correlations during 1 min home cage recording. No significant differences, two-way ANOVA followed by Sidak's test. Data are mean ± SEM.

(F) Pairwise Pearson's correlations during each task phase for C57 and CC012 (n = 7 ea). Individual trials shown in Figure S6C at 10 trials/mouse. Individual mice shown, including mean ± SEM. *p < 0.05, **p < 0.01, ***p < 0.001 by two-way ANOVA with repeated measures and Sidak's multiple comparisons.

(G) Pairwise Pearson's correlations during each task phase for mdTH-Gpr12 overexpression (Gpr12OE) and RFP (RFP) control injection (n = 8 ea). Individual trials shown in Figure S6F at 10 trials/mouse. Individual mice shown, including mean ± SEM. *p < 0.05, **p < 0.01, ***p < 0.001 by two-way ANOVA with repeated measures and Sidak's multiple comparisons test.

(H) The combined correlations of encoding and delay phases were separated by correct and incorrect trials. n = 16 mice, 10 trials per mouse, p < 0.001, Welch's t test.

(I) Averaged *Z* scored PFC GCaMP6f activity on correct and incorrect trials. Individual data points show, including mean. ****p(C'D) < 0.0001, Sidak's multiple comparisons.

(J) Suggested model of working memory consistent with the data: brief bouts of persistent activity, in thalamocortical neurons, interleaved with periods of short-term plasticity.

See also Figures S5 and S6.

Please cite this article in press as: Hsiao et al., A Thalamic Orphan Receptor Drives Variability in Short-Term Memory, Cell (2020), https://doi.org/10.1016/j.cell.2020.09.011

CellPress

ACKNOWLEDGMENTS

We are grateful to Leslie Vosshall, Andy Clark, Marybeth Hatten, Bob Darnell, Brian Bennett, Samir Kelada, Conor Liston, Zach Gershon, and Andrew Toader for helpful discussions related to the project or critical reading of the manuscript. We also thank Kristen Pleil, Joshua Levitz, and Bailey Peck for discussions related to thalamic physiology, GPCR biology, and DO genetic mapping, respectively. For this work, K.H. is supported by a Robertson Therapeutic Development Fund and P.R. is supported by the National Institutes of Health under award number DP2AG058487 and by the NIMH of the National Institutes of Health under award number R00MH109652.

AUTHOR CONTRIBUTIONS

P.R. and P.S. conceived the study. K.H., P.R., and P.S. designed the experiments. K.H. performed behavioral testing, molecular studies related to RNA-seq, qPCR, generation and validation of RNAi constructs, and CRISPR-knockout lines, as well as photometry experiments during behavior, with supervision by P.R. C.N. assisted with histology, photometry, behavioral testing, and analyses. W.P. performed haplotype reconstructions, QTL analyses, and RNA-seq analyses, with assistance from M.K. and G.R.K. and supervision by P.S. N.Y. designed and performed analyses for *in vitro* calcium imaging and *in vivo* photometry recordings. S.K. designed and built the custom multi-fiber photometry rig together with custom scripts for acquiring and post-processing the data. A.T. performed ISH experiments and assisted with surgeries. T.C. and C.C.-N. performed phenotyping of the initial DO cohort, supervised by R.T. P.R. and K.H. wrote the paper with input from all authors.

DECLARATION OF INTERESTS

The authors declare no competing interests.

Received: October 31, 2019
Revised: June 9, 2020
Accepted: September 1, 2020
Published: September 29, 2020

REFERENCES

Akrami, A., Kopec, C.D., Diamond, M.E., and Brody, C.D. (2018). Posterior parietal cortex represents sensory history and mediates its effects on behaviour. Nature *554*, 368–372.

Arnsten, A.F., and Jin, L.E. (2014). Molecular influences on working memory circuits in dorsolateral prefrontal cortex. Prog. Mol. Biol. Transl. Sci. *122*, 211–231.

Baddeley, A. (2003). Working memory: looking back and looking forward. Nat. Rev. Neurosci. *4*, 829–839.

Baddeley, A. (2012). Working memory: theories, models, and controversies. Annu. Rev. Psychol. *63*, 1–29.

Baddeley, A.D., and Hitch, G. (1974). Working Memory. Psychology of Learning & Motivation *8*, 47–89.

Barak, O., and Tsodyks, M. (2014). Working models of working memory. Curr. Opin. Neurobiol. *25*, 20–24.

Bargiello, T.A., Jackson, F.R., and Young, M.W. (1984). Restoration of circadian behavioural rhythms by gene transfer in Drosophila. Nature *312*, 752–754.

Bolkan, S.S., Stujenske, J.M., Parnaudeau, S., Spellman, T.J., Rauffenbart, C., Abbas, A.I., Harris, A.Z., Gordon, J.A., and Kellendonk, C. (2017). Thalamic projections sustain prefrontal activity during working memory maintenance. Nat. Neurosci. *20*, 987–996.

Brody, C.D., Romo, R., and Kepecs, A. (2003). Basic mechanisms for graded persistent activity: discrete attractors, continuous attractors, and dynamic representations. Curr. Opin. Neurobiol. *13*, 204–211.

Broman, K.W., Gatti, D.M., Simecek, P., Furlotte, N.A., Prins, P., Sen, Ś., Yandell, B.S., and Churchill, G.A. (2019). R/qtl2: Software for mapping quantitative trait loci with high-dimensional data and multiparent populations. Genetics *211*, 495–502.

Buzsáki, G., Geisler, C., Henze, D.A., and Wang, X.J. (2004). Interneuron Diversity series: Circuit complexity and axon wiring economy of cortical interneurons. Trends Neurosci. *27*, 186–193.

Carmody, R.N., Gerber, G.K., Luevano, J.M., Jr., Gatti, D.M., Somes, L., Svenson, K.L., and Turnbaugh, P.J. (2015). Diet dominates host genotype in shaping the murine gut microbiota. Cell Host Microbe *17*, 72–84.

Chen, E.Y., Tan, C.M., Kou, Y., Duan, Q., Wang, Z., Meirelles, G.V., Clark, N.R., and Ma'ayan, A. (2013). Enrichr: interactive and collaborative HTML5 gene list enrichment analysis tool. BMC Bioinformatics *14*, 128.

Chick, J.M., Munger, S.C., Simecek, P., Huttlin, E.L., Choi, K., Gatti, D.M., Raghupathy, N., Svenson, K.L., Churchill, G.A., and Gygi, S.P. (2016). Defining the consequences of genetic variation on a proteome-wide scale. Nature *534*, 500–505.

Choi, H.M.T., Chang, J.Y., Trinh, A., Padilla, J.E., Fraser, S.E., and Pierce, N.A. (2010). Programmable in situ amplification for multiplexed imaging of mRNA expression. Nat. Biotechnol. *28*, 1208–1212.

Churchill, G.A., Airey, D.C., Allayee, H., Angel, J.M., Attie, A.D., Beatty, J., Beavis, W.D., Belknap, J.K., Bennett, B., Berrettini, W., et al.; Complex Trait Consortium (2004). The Collaborative Cross, a community resource for the genetic analysis of complex traits. Nat. Genet. *36*, 1133–1137.

Churchill, G.A., Gatti, D.M., Munger, S.C., and Svenson, K.L. (2012). The Diversity Outbred mouse population. Mamm. Genome *23*, 713–718.

Coffey, A.R., Kanke, M., Smallwood, T.L., Albright, J., Pitman, W., Gharaibeh, R.Z., Hua, K., Gertz, E., Biddinger, S.B., Temel, R.E., et al. (2019). microRNA-146a-5p association with the cardiometabolic disease risk factor TMAO. Physiol. Genomics *51*, 59–71.

Constantinidis, C., and Procyk, E. (2004). The primate working memory networks. Cogn. Affect. Behav. Neurosci. *4*, 444–465.

Conway, A.R., Kane, M.J., and Engle, R.W. (2003). Working memory capacity and its relation to general intelligence. Trends Cogn. Sci. *7*, 547–552.

Cui, G., Jun, S.B., Jin, X., Pham, M.D., Vogel, S.S., Lovinger, D.M., and Costa, R.M. (2013). Concurrent activation of striatal direct and indirect pathways during action initiation. Nature *494*, 238–242.

Dash, P.K., Moore, A.N., Kobori, N., and Runyan, J.D. (2007). Molecular activity underlying working memory. Learn. Mem. *14*, 554–563.

de Bono, M., and Bargmann, C.I. (1998). Natural variation in a neuropeptide Y receptor homolog modifies social behavior and food response in C. elegans. Cell *94*, 679–689.

Dias, R., and Aggleton, J.P. (2000). Effects of selective excitotoxic prefrontal lesions on acquisition of nonmatching- and matching-to-place in the T-maze in the rat: differential involvement of the prelimbic-infralimbic and anterior cingulate cortices in providing behavioural flexibility. Eur. J. Neurosci. *12*, 4457–4466.

Dobin, A., Davis, C.A., Schlesinger, F., Drenkow, J., Zaleski, C., Jha, S., Batut, P., Chaisson, M., and Gingeras, T.R. (2013). STAR: ultrafast universal RNA-seq aligner. Bioinformatics *29*, 15–21.

Drago, A., and Kure Fischer, E. (2018). A molecular pathway analysis informs the genetic risk for arrhythmias during antipsychotic treatment. Int. Clin. Psychopharmacol. *33*, 1–14.

Dudai, Y., Jan, Y.N., Byers, D., Quinn, W.G., and Benzer, S. (1976). dunce, a mutant of Drosophila deficient in learning. Proc. Natl. Acad. Sci. USA *73*, 1684–1688.

Dudchenko, P.A. (2004). An overview of the tasks used to test working memory in rodents. Neurosci. Biobehav. Rev. *28*, 699–709.

Egorov, A.V., Hamam, B.N., Fransén, E., Hasselmo, M.E., and Alonso, A.A. (2002). Graded persistent activity in entorhinal cortex neurons. Nature *420*, 173–178.

Erlich, J.C., Bialek, M., and Brody, C.D. (2011). A cortical substrate for memory-guided orienting in the rat. Neuron *72*, 330–343.

Fujisawa, S., Amarasingham, A., Harrison, M.T., and Buzsáki, G. (2008). Behavior-dependent short-term assembly dynamics in the medial prefrontal cortex. Nat. Neurosci. *11*, 823–833.

Funahashi, S., Chafee, M.V., and Goldman-Rakic, P.S. (1993). Prefrontal neuronal activity in rhesus monkeys performing a delayed anti-saccade task. Nature *365*, 753–756.

Fuster, J.M., and Alexander, G.E. (1971). Neuron activity related to short-term memory. Science *173*, 652–654.

Goldman-Rakic, P.S. (1995). Cellular basis of working memory. Neuron *14*, 477–485.

Guo, Z.V., Inagaki, H.K., Daie, K., Druckmann, S., Gerfen, C.R., and Svoboda, K. (2017). Maintenance of persistent activity in a frontal thalamocortical loop. Nature *545*, 181–186.

Harris, A.Z., and Gordon, J.A. (2015). Long-range neural synchrony in behavior. Annu. Rev. Neurosci. *38*, 171–194.

Harvey, C.D., Coen, P., and Tank, D.W. (2012). Choice-specific sequences in parietal cortex during a virtual-navigation decision task. Nature *484*, 62–68.

Howe, J.R., 6th, Bear, M.F., Golshani, P., Klann, E., Lipton, S.A., Mucke, L., Sahin, M., and Silva, A.J. (2018). The mouse as a model for neuropsychiatric drug development. Curr. Biol. *28*, R909–R914.

Jacobsen, C. (1936). Studies of cerebral function in primates. Comparative Psychology Monographs *13*, 3–60.

Kang, H.M., Sul, J.H., Service, S.K., Zaitlen, N.A., Kong, S.Y., Freimer, N.B., Sabatti, C., and Eskin, E. (2010). Variance component model to account for sample structure in genome-wide association studies. Nat. Genet. *42*, 348–354.

Katz, L.C., and Shatz, C.J. (1996). Synaptic activity and the construction of cortical circuits. Science *274*, 1133–1138.

Keele, G.R., Quach, B.C., Israel, J.W., Chappell, G.A., Lewis, L., Safi, A., Simon, J.M., Cotney, P., Crawford, G.E., Valdar, W., et al. (2020). Integrative QTL analysis of gene expression and chromatin accessibility identifies multi-tissue patterns of genetic regulation. PLoS Genet. *16*, e1008537.

Kim, C.K., Yang, S.J., Pichamoorthy, N., Young, N.P., Kauvar, I., Jennings, J.H., Lerner, T.N., Berndt, A., Lee, S.Y., Ramakrishnan, C., et al. (2016). Simultaneous fast measurement of circuit dynamics at multiple sites across the mammalian brain. Nat. Methods *13*, 325–328.

Knowles, E.E.M., Mathias, S.R., McKay, D.R., Sprooten, E., Blangero, J., Almasy, L., and Glahn, D.C. (2014). Genome-wide analyses of working memory ability: a review. Curr. Behav. Neurosci. Rep. *1*, 224–233.

Kupferschmidt, D.A., and Gordon, J.A. (2018). The dynamics of disordered dialogue: Prefrontal, hippocampal and thalamic miscommunication underlying working memory deficits in schizophrenia. Brain Neurosci. Adv. *2*, 2398212818771821.

Lalonde, R. (2002). The neurobiological basis of spontaneous alternation. Neurosci. Biobehav. Rev. *26*, 91–104.

Lee, J.J., Wedow, R., Okbay, A., Kong, E., Maghzian, O., Zacher, M., Nguyen-Viet, T.A., Bowers, P., Sidorenko, J., Karlsson Linnér, R., et al.; 23andMe Research Team; COGENT (Cognitive Genomics Consortium); Social Science Genetic Association Consortium (2018). Gene discovery and polygenic prediction from a genome-wide association study of educational attainment in 1.1 million individuals. Nat. Genet. *50*, 1112–1121.

Lein, E.S., Hawrylycz, M.J., Ao, N., Ayres, M., Bensinger, A., Bernard, A., Boe, A.F., Boguski, M.S., Brockway, K.S., Byrnes, E.J., et al. (2007). Genome-wide atlas of gene expression in the adult mouse brain. Nature *445*, 168–176.

Lim, S., and Goldman, M.S. (2013). Balanced cortical microcircuitry for maintaining information in working memory. Nat. Neurosci. *16*, 1306–1314.

Loewenstein, Y., Mahon, S., Chadderton, P., Kitamura, K., Sompolinsky, H., Yarom, Y., and Häusser, M. (2005). Bistability of cerebellar Purkinje cells modulated by sensory stimulation. Nat. Neurosci. *8*, 202–211.

Love, M.I., Huber, W., and Anders, S. (2014). Moderated estimation of fold change and dispersion for RNA-seq data with DESeq2. Genome Biology *15*, 550.

Miller, E.K., Li, L., and Desimone, R. (1993). Activity of neurons in anterior inferior temporal cortex during a short-term memory task. J. Neurosci. *13*, 1460–1478.

Miller, E.K., Lundqvist, M., and Bastos, A.M. (2018). Working Memory 2.0. Neuron *100*, 463–475.

Morales, P., Isawi, I., and Reggio, P.H. (2018). Towards a better understanding of the cannabinoid-related orphan receptors GPR3, GPR6, and GPR12. Drug Metab. Rev. *50*, 74–93.

Nicod, J., Davies, R.W., Cai, N., Hassett, C., Goodstadt, L., Cosgrove, C., Yee, B.K., Lionikaite, V., McIntyre, R.E., Remme, C.A., et al. (2016). Genome-wide association of multiple complex traits in outbred mice by ultra-low-coverage sequencing. Nat. Genet. *48*, 912–918.

Nuzhdin, S.V., Pasyukova, E.G., Dilda, C.L., Zeng, Z.B., and Mackay, T.F. (1997). Sex-specific quantitative trait loci affecting longevity in Drosophila melanogaster. Proc. Natl. Acad. Sci. USA *94*, 9734–9739.

Parker, C.C., Gopalakrishnan, S., Carbonetto, P., Gonzales, N.M., Leung, E., Park, Y.J., Aryee, E., Davis, J., Blizard, D.A., Ackert-Bicknell, C.L., et al. (2016). Genome-wide association study of behavioral, physiological and gene expression traits in outbred CFW mice. Nat. Genet. *48*, 919–926.

Parnaudeau, S., O'Neill, P.K., Bolkan, S.S., Ward, R.D., Abbas, A.I., Roth, B.L., Balsam, P.D., Gordon, J.A., and Kellendonk, C. (2013). Inhibition of mediodorsal thalamus disrupts thalamofrontal connectivity and cognition. Neuron *77*, 1151–1162.

Patro, R., Duggal, G., Love, M.I., Irizarry, R.A., and Kingsford, C. (2017). Salmon provides fast and bias-aware quantification of transcript expression. Nature Methods *14*, 417–419.

Quinn, W.G., Sziber, P.P., and Booker, R. (1979). The Drosophila memory mutant amnesiac. Nature *277*, 212–214.

Raghavan, N.S., Brickman, A.M., Andrews, H., Manly, J.J., Schupf, N., Lantigua, R., Wolock, C.J., Kamalakaran, S., Petrovski, S., Tosto, G., et al.; Alzheimer's Disease Sequencing Project (2018). Whole-exome sequencing in 20,197 persons for rare variants in Alzheimer's disease. Ann. Clin. Transl. Neurol. *5*, 832–842.

Rajasethupathy, P., Sankaran, S., Marshel, J.H., Kim, C.K., Ferenczi, E., Lee, S.Y., Berndt, A., Ramakrishnan, C., Jaffe, A., Lo, M., et al. (2015). Projections from neocortex mediate top-down control of memory retrieval. Nature *526*, 653–659.

Romo, R., Brody, C.D., Hernández, A., and Lemus, L. (1999). Neuronal correlates of parametric working memory in the prefrontal cortex. Nature *399*, 470–473.

Rue, H., Martino, S., and Chopin, N. (2009). Approximate Bayesian inference for latent Gaussian models by using integrated nested Laplace approximations. Journal of the Royal Statistical Society: Series B*71*, pp. 319–392.

Saul, M.C., Philip, V.M., Reinholdt, L.G., and Chesler, E.J.; Center for Systems Neurogenetics of Addiction (2019). High-diversity mouse populations for complex traits. Trends Genet. *35*, 501–514.

Saunders, A., Macosko, E.Z., Wysoker, A., Goldman, M., Krienen, F.M., de Rivera, H., Bien, E., Baum, M., Bortolin, L., Wang, S., et al. (2018). Molecular diversity and specializations among the cells of the adult mouse brain. Cell *174*, 1015–1030.e16.

Schmitt, L.I., Wimmer, R.D., Nakajima, M., Happ, M., Mofakham, S., and Halassa, M.M. (2017). Thalamic amplification of cortical connectivity sustains attentional control. Nature *545*, 219–223.

Song, Z.H., Modi, W., and Bonner, T.I. (1995). Molecular cloning and chromosomal localization of human genes encoding three closely related G protein-coupled receptors. Genomics *28*, 347–349.

Tarantino, L.M., and Bucan, M. (2000). Dissection of behavior and psychiatric disorders using the mouse as a model. Hum. Mol. Genet. *9*, 953–965.

Thuault, S.J., Malleret, G., Constantinople, C.M., Nicholls, R., Chen, I., Zhu, J., Panteleyev, A., Vronskaya, S., Nolan, M.F., Bruno, R., et al. (2013). Prefrontal cortex HCN1 channels enable intrinsic persistent neural firing and executive memory function. J. Neurosci. *33*, 13583–13599.

Uhlenbrock, K., Gassenhuber, H., and Kostenis, E. (2002). Sphingosine 1-phosphate is a ligand of the human gpr3, gpr6 and gpr12 family of constitutively active G protein-coupled receptors. Cell. Signal. *14*, 941–953.

Wang, M., Ramos, B.P., Paspalas, C.D., Shu, Y., Simen, A., Duque, A., Vijayraghavan, S., Brennan, A., Dudley, A., Nou, E., et al. (2011). Alpha 2A-adrenoceptors strengthen working memory networks by inhibiting cAMP-HCN channel signaling in prefrontal cortex. Cell *129*, 397–410.

Xiao, M.F., Xu, D., Craig, M.T., Pelkey, K.A., Chien, C.C., Shi, Y., Zhang, J., Resnick, S., Pletnikova, O., Salmon, D., et al. (2017). NPTX2 and cognitive dysfunction in Alzheimer's Disease. eLife *6*, 23798.

Zhang, Z., Wang, W., and Valdar, W. (2014). Bayesian modeling of haplotype effects in multiparent populations. Genetics *198*, 139–156.

Zylberberg, J., and Strowbridge, B.W. (2017). Mechanisms of Persistent Activity in Cortical Circuits: Possible Neural Substrates for Working Memory. Annu. Rev. Neurosci. *40*, 603–627.

Please cite this article in press as: Hsiao et al., A Thalamic Orphan Receptor Drives Variability in Short-Term Memory, Cell (2020), https://doi.org/10.1016/j.cell.2020.09.011

STAR★METHODS

KEY RESOURCES TABLE

REAGENT or RESOURCE	SOURCE	IDENTIFIER
Antibodies		
mouse monoclonal anti-Tubulin	Covance	MMS-435P, RRID:AB_2313773
mouse monoclonal anti-V5 tag	Thermo Fisher Scientific	R960-25, RRID:AB_2556564
guinea pig polyclonal anti-Parvalbumin	SWANT	GP72, RRID:AB_2665495
rabbit polyclonal anti-Gpr12	AVIVA	Cat# ARP64695_P050
IRDye 800CW anti-mouse	Li-Cor	926-68070, RRID:AB_10956588
IRDye 680RD anti-rabbit	Li-Cor	925-68073, RRID:AB_2716687
Donkey anti-rabbit Rhodamine Red-X	Jackson ImmunoResearch	711-296-152, RRID:AB_2340614
Donkey anti-mouse Alexa488	Jackson ImmunoResearch	715-546-150, RRID:AB_2340849
Donkey anti-guinea pig Alexa647	Jackson ImmunoResearch	706-606-148, RRID:AB_2340477
Bacterial and Virus Strains		
AAV1-CaMKIIa-GCaMP6f	A gift from James M. Wilson	Addgene viral prep # 100834-AAV1
AAV1-CAG-GCaMP6f	A gift from Douglas Kim & GENIE Project	Addgene viral prep # 100836-AAV1
rgAAV-GFP	A gift from Edward Boyden	Addgene viral prep # 37825-AAVrg
Custom AAV-mediated RNAi	Vigene Biosciences	N/A
Custom AAV-mediated gene expression	Boston Children's Hospital Viral Core	N/A
Chemicals, Peptides, and Recombinant Proteins		
Nifedipine	Tocris	1075; CAS#21829-25-4
ZD 7288	Tocris	1000; CAS# 133059-99-1
Z 944	Tocris	6367; CAS# 1199236-64-0
L-glutamic acid	Sigma-Aldrich	RES5063G-A701X; CAS#6106-04-3
Cal520-AM dye	Aat Bioquest	21131
Critical Commercial Assays		
Total RNA Purification Kit	NORGEN	17200
TruScript First Strand cDNA Synthesis Kit	NORGEN	54420
TruSeq stranded mRNA LT kit	Illumina	Cat# RS-122-2101
ProteoExtract	Calbiochem	Cat#71772-3
Deposited Data		
RNA-seq Raw and analyzed data	This paper	GEO: GSE156836
Experimental Models: Cell Lines		
Mouse: HT-22 cells	Sigma	SCC129
Experimental Models: Organisms/Strains		
Mouse: C57BL/6J	Jackson Laboratories	IMSR Cat# JAX:000664, RRID:IMSR_JAX:000664
Mouse: CC004/TauUncJ	Jackson Laboratories	IMSR Cat# JAX:020944, RRID:IMSR_JAX:020944
Mouse: CC012/GeniUncJ	Jackson Laboratories	IMSR Cat# JAX:028409, RRID:IMSR_JAX:028409
Mouse: CC046/Unc	Systems Genetics Core Facility, UNC	IMSR Cat# UNC:156, RRID:IMSR_UNC:156
Oligonucleotides		
qPCR primers of mouse *Nptx2, Ube2d2a, Grid2ip, Gpr12, Tubulin, Cacna1c, Cacna1c*	Table S2, This paper	N/A
RNAi targeting sequence of mouse *Gpr12, Tmem130, Nptx2*	Table S2, This paper	N/A
CRISPR gRNA targeting mouse *Gpr12*	Table S2, This paper	N/A

(*Continued on next page*)

Please cite this article in press as: Hsiao et al., A Thalamic Orphan Receptor Drives Variability in Short-Term Memory, Cell (2020), https://doi.org/10.1016/j.cell.2020.09.011

Continued

REAGENT or RESOURCE	SOURCE	IDENTIFIER
Recombinant DNA		
EF1a-T7-hspCas9-T2A-RFP-H1-gRNA Cloning Vector	SystemBiosciences	CAS701R-1
pSpCas9(BB)-2A-Puro	A gift from Feng Zhang; Ran et al.,2013	Addgene plasmid # 48139 ; http://addgene.org/48139; RRID:Addgene_48139
pAV-U6-RFP	Vigene Biosciences	P100038
pAAV-hSyn-mCherry	A gift from Karl Deisseroth	Addgene plasmid # 114472 ;http://addgene.org/114472; RRID:Addgene_114472
Software and Algorithms		
MATLAB	The MathWorks	RRID:SCR_001622
Fiji (ImageJ)	NIH	RRID: SCR_003070
Ethovision XT	Noldus Information Technology	RRID: SCR_000441
DESeq2 v1.22	Love et al., 2014	https://bioconductor.org/packages/release/bioc/html/DESeq2.html
STAR v2.5.3a	Dobin et al., 2013	https://github.com/alexdobin/STAR/archive/2.5.3a.tar.gz
Salmon v0.8.2	Patro et al., 2017	https://github.com/COMBINE-lab/salmon/archive/v0.8.2.tar.gz
R v3.5.0	The R Project for Statistical Computing	https://www.r-project.org/
Enrichr	Chen et al., 2013	https://maayanlab.cloud/Enrichr/
R package miQTL	Keele et al., 2020	https://github.com/gkeele/miqtl
Mix-Model Association R/qtl2	Kang et al., 2010	http://genetics.cs.ucla.edu/emmax
Diploffect linear mixed model (LMM)	Zhang et al., 2014	File S2, https://www.genetics.org/lookup/suppl/doi:10.1534/genetics.114.166249/-/DC1/genetics.114.166249-2.zip
Odyssey 3.0	LI-COR Biosciences	RRID: SCR_014579
LightCycler	Roche Life Science	RRID: SCR_012155
FreezeFrame	Coulburn, USA	RRID:SCR_014429

RESOURCE AVAILABILITY

Lead Contact

Further information and requests for resources and reagents should be directed to and will be fulfilled by the Lead Contact, Priyamvada Rajasethupathy (priya@rockefeller.edu).

Materials Availability

All other unique reagents generated in this study are available from the Lead Contact with a completed Materials Transfer Agreement.

Data and Code Availability

The accession number for the sequencing data reported in this paper is GEO: GSE156836/ https://www.ncbi.nlm.nih.gov/geo/query/acc.cgi?acc=GSE156836. Numerical data for each figure are included with the manuscript as source data. All other data are available from the corresponding author upon reasonable request. Custom MATLAB code are available upon request from the Lead Contact.

EXPERIMENTAL MODEL AND SUBJECT DETAILS

All procedures were done in accordance with guidelines approved by the Institutional Animal Care and Use Committees (protocol #17002) at The Rockefeller University.

Mice

All animals were purchased from The Jackson Laboratory. Diversity Outbred (DO) mice were obtained from the 25th generation of the population. Mice were aged 8 weeks (DO mice and Collaborative Cross [CC] lines phenotyping), 10 weeks (photometry cohorts), or 12-15 weeks (RNAi and Overexpression cohorts) for various experiments and housed under a 12 h light–dark cycle in a temperature-

Please cite this article in press as: Hsiao et al., A Thalamic Orphan Receptor Drives Variability in Short-Term Memory, Cell (2020), https://doi.org/10.1016/j.cell.2020.09.011

controlled environment with access to food and water anytime. Mice were single housed for DO phenotyping and group housed with littermates (4 mice/cage) for all other behavioral cohorts. DO phenotyping was performed with all males to sufficiently power the study at affordable cost, but future studies will use female-only or mixed cohorts. For DO phenotyping, of initial 200 mice purchased, 193 were phenotyped in spontaneous alternation (7 died), and of these, 182 were used for QTL mapping (another 11 did not perform the task). For Delay non-Match to Place (DNMP) behavioral training and testing, mice were food-restricted (CC phenotyping, RNAi and Overexpression cohorts) or water-restricted (photometry cohort) and maintained at 85% of their initial weight.

METHOD DETAILS

QTL mapping in Diversity Outbred Mice

Genotype Identification & Haplotype Reconstruction

SNP locations and genotypes for the eight founder strains were acquired from ftp.jax.org/MUGA and the consensus genotype for each founder strain and each SNP was determined from the multiple individuals that were genotyped. SNP genotypes for the 182 DO mice were determined using a high density mouse universal genotyping array, GigaMUGA (geneSeek). A total of 114,184 SNPs were detected on the 19 autosomes and X chromosomes. Using R/qtl2 (Broman et al., 2019), founder haplotype probabilities were reconstructed for all samples and then converted to additive allelic dosages and scaled to 1. Realized genetic relationship matrices, often referred to as kinship matrices, were estimated using the leave one chromosome out (LOCO) method, so that the kinship term does not absorb variation explained by the putative QTL. Another QTL mapping software package for multi-parental populations (MPP), miQTL (Keele et al., 2020), was used to confirm findings from R/qtl2, and to visualize and assess the level of heterozygosity at the locus of interest.

Heritability estimation

Heritability is the ratio of the variance component corresponding to the kinship term over the sum of the kinship variance component and the noise variance i.e., the proportion of variance explained by genetic factors. Heritability for the phenotype of interest in this DO cohort was estimated using a Bayesian linear mixed model (Rue et al., 2009), which is appealing because of the ease by which it provides interval estimates. The phenotype was centered and scaled, and modeled as a linear function of the random kinship term representing the correlation structure encoded in the genetic relationship matrix (often referred to as the kinship matrix), and an unstructured error term.

QTL Mapping

Phenotype values from the spontaneous alternation test (% alternation) were subject to Box-Cox transformation. Then, using R/qtl2, an additive single locus linear mixed model was fit at positions across the genome, producing a genome scan. Potential population structure was controlled for through the inclusion of a random effect to account for correlation structure measured by the kinship matrix. This was performed in R/qtl2 using the leave one chromosome out (LOCO) method (Kang et al., 2010). For confirmation of the QTL results, we performed a multiple imputation genome scan (11 imputations) using miQTL (Keele et al., 2020), to assess whether uncertainty in founder haplotype reconstruction was strongly influencing the results. Genome-wide significance thresholds (alpha = 0.05) for the genome scans were determined through 1000 permutations of the diplotype.

Analysis of Founder Contributions

To determine the founder haplotype effects driving *Smart1*, we first estimated best linear unbiased predictors (BLUPs), which constrain potentially unstable effects by fitting the QTL term as a random effect. To further confirm these results, we used Diploffect (Zhang et al., 2014), to estimate posterior credible intervals for the haplotype effects as well as the proportion of variance explained by the QTL (sometimes referred to as the locus heritability).

Animal Behaviors

Spontaneous alternation T-maze

Tests were conducted in the T-maze with the following arm dimensions: 12 × 3 x 5 in (L x W x H) and recorded using a ceiling-mounted camera under red light illumination. Testing consisted of a single 5 min trial, in which the mouse was allowed to explore all three arms of the T-maze. Mice were acclimatized to the experimental site for 1 h before all experiments. The experimenter was blind to the viral condition of all mice during behavioral testing, but were unable to be blinded to identity when testing C57 (black) versus CC012 (gray) mice because of the difference in their coat color. We timed latency to leave the start box and if it exceeds 3 min, mice are pushed out with a pen. Entries into each arm were tracked: start arm is M, left (bottom) arm is L, right (top) arm is R (Table S1). Sequences of arm entries were manually recorded from video recording (DO phenotyping) or automatically tracked by EthoVision XT (Noldus) software (Collaborative Cross lines, RNAi, and Overexpression cohorts). Percentage alternation [%] was defined as consecutive entries in 3 different arms, divided by the number of possible alternations (total arm entries minus 2. A direct revisit (ie., MM) or an indirect revisit (ie., MLM) to an arm was classified as an incorrect alternation. Percentage error [%] was calculated as the ratio of incorrect alternations to total alternations. Mice with less than 8 arm entries during the 5 min trial were excluded from analysis.

Percentage alternation scores were then compared to: the total number of arm entries, total distance traveled, latency to first goal arm entry, stereotypy, and performance on a contextual fear-conditioning task, to determine if performance was influenced by factors that may confound working memory performance such as gross motor, motivational, or sensory deficits respectively. The

Please cite this article in press as: Hsiao et al., A Thalamic Orphan Receptor Drives Variability in Short-Term Memory, Cell (2020), https://doi.org/10.1016/j.cell.2020.09.011

stereotypy index was defined as the number of counter-clockwise alternation triplets (RLM, LMR, MRL) subtracted from the number of clockwise triplets (LRM, RML, MLR), divided by the total number of correct alternations.

Delayed Non-Match to Place (DNMP)

Testing was conducted using the same T-maze as described in the spontaneous alternation test. Mice were gradually food restricted to 85% of their body weight at 8 weeks age (Collaborative Cross lines) or 2-6 weeks after viral injection/ cannula implantation surgeries (photometry, RNAi, and Overexpression cohorts). Habituation systemically reduces novelty and exploratory-drives to confound working memory assessment. Mice were first habituated to the T-maze over 2-3 d before DNMP training. During habituation, mice were allowed to freely explore the maze, where 20mg chocolate pellets (AIN-76A, TestDiet) were placed in an octagonal dish at the end of each arm, for 20-30 min with their cage-mates (CC mice, RNAi, and Overexpression cohorts), or while tethered to optical fibers and/or the recording tether (photometry cohort). On the subsequent 5-6 days mice underwent DNMP training, which consisted of 10 trials per day. Each trial consisted of two phases, a forced choice followed by a free choice. At the beginning of each trial, a small octagonal dish with a chocolate pellet was deposited at the end of each goal arm, and a sliding guillotine door was positioned to block entry to either the left or right goal arm in a pseudorandom order. For the forced choice run, the mouse was placed at the base of the T-maze and allowed to obtain the pellet from the open, baited arm before returning to and being enclosed in the start box. After a 10 s delay period, in which both arms were made accessible, the mouse was released to enter the arm of choice. Sample arm runs were pseudo-randomly selected on a trial-by-trial basis. A trial was considered correct if the mouse entered the goal arm not visited during the forced choice and was able to collect the pellet, and incorrect if they revisited the same arm, where they were confined without reward for 20 s. In the photometry cohort, mice were water deprived and trained to receive a 20 μL water drop reward, instead of chocolate pellet. In addition, photometry mice were tethered to optical fibers on training days 3-5. Daily training continued until mice reached criterion performance, defined as 2 consecutive days above 70% without displaying a strong arm preference (mice that didn't meet criterion were excluded from subsequent studies, except for Gpr12RNAi injected CC012 cohort where due to the ceiling effect for low performers, no mice were excluded). Mice with extreme day-to-day variability during training were also excluded from subsequent analysis (demonstrated by significant deviations from the 90% prediction interval of a best-fit line of reference from c57 mice, n = 17). One day after completion of DNMP training, mice were tested on 10 trials at an extended delay period of 20 s and the following day at 30 s (45 s was also tested in the photometry cohort). The experimenter was blind to the viral treatments (ie. targeted RNAi, overexpression, scramble RNAi, or mCherry) of mice during behavioral testing. For photometry experiments, testing at the 45 s delay occurred over two days to collect more trials and minimize bleaching of GCaMP fluorescence. All behavior was conducted during the light cycle.

Object Place Memory

The object-place memory arena consisted of a square box (16"Wx16"Dx14"H). The subject's ability to recognize that an object that it had experienced before had changed location was assessed. Mice habituated to an empty arena for 10 min. ahead of each phase. In the training phase, mice were exposed to objects F1 and F2 (F: familiar), which were placed in the far corners of the arena, with an internal cue (and marked with lab tape). The animal was allowed to explore both objects during two sample sessions of 5 min, with an inter-session interval of 5 min. In between each trial, the mouse was removed from the box and placed in the home cage while the box was cleaned with 10% Ethanol and then water. All objects were cleaned with 10% Ethanol and then water after trials. After a delay of 24 h, the testing phase began. In the testing phase, object F1 was placed in the same position, while object F2 was placed in the midway-to-corner adjacent to the original position (N, novel place), so that the two objects F1 and N were at least 30° juxtaposed. Mice were placed into the arena facing opposite toward the wall with internal cue and objects, and allowed to freely explore the environment and the objects for 5 min. Time spent exploring the displaced and non-displaced objects was measured. The identity of the objects as well as the spatial location in which the objects were located was balanced between subjects. After 24 h, mice were placed back in the arena for the 2nd testing phase, again facing opposite toward the wall with internal cue and objects. The two objects were present, object F1 was now displaced to a novel spatial (N1) location while the other (F2) stayed at the same place as in the first testing day. Mice were again allowed to freely explore the environment and the objects for 5 min. The discrimination index (DI) used to assess memory performance was calculated as the difference in time exploring the novel object location and stable location divided by the total exploration time. This results in a score ranging from −1 (preference for the stable location) to +1 (preference for the moving object location). A score of 0 indicates no preference for either object location.

Fear Conditioning

The fear conditioning chamber consisted of a square conditioning cage (7"Wx7"Dx12"H) with a grid floor wired to a shock generator and a scrambler, with a house light, and encompassed in an acoustic chamber (Coulburn Instruments, PA, USA). Mice were first habituated in this chamber for 120 s. Subsequently, fear conditioning was performed by placing mice in the conditioning cage (visual cues: bare walls; tactile cues: grid floor; house light off), while receiving three 2 s shock pulses of 7 mA at 90 s, 120 s, and 150 s with house light continuously on. Mice stayed in the conditioning chamber for an additional 60 s before returning to the home cage. Approximately 24 h later, memory retrieval was tested by returning mice to the original chamber for 3.5 min in the absence of any shocks. The chamber was cleaned with 10% alcohol after each subject was trained or tested. Freezing behavior on training and retrieval days were recorded and analyzed offline using the automated motion detection software FreezeFrame (Coulburn, USA) and fear memory was assessed as percentage time spent freezing in the last 2 min of the retrieval session.

Please cite this article in press as: Hsiao et al., A Thalamic Orphan Receptor Drives Variability in Short-Term Memory, Cell (2020), https://doi.org/10.1016/j.cell.2020.09.011

Animal Surgical Procedures

Surgical procedures and viral injections were carried out under protocols approved by Rockefeller University IACUC and were performed in mice anesthetized with 1%–2% isoflurane using a stereotactic apparatus (Kopf). In RNAi experiments, C57 or CC012 mice were bilaterally injected in the mdTh or PFC with an AAV9 expressing either scramble (non-targeting) RNAi-RFP or targeted RNAi-RFP (ie. *Gpr12, Tmem130, Nptx2 RNAi*) constructs under the U6 promoter at a volume of 1.0 μL (0.1 μL/min). In gene expression experiments, mice were bilaterally injected in the mdTh with AAV9 expressing either mCherry or Grid2ip-t2A-tdTomato or Gpr12-ires-tdTomato construct under the human Synapsin (hSYN) promoter at a volume of 1.0 μL. In TC retrograde tracing experiments, an rgAAV expressing eGFP under the chicken β-actin (CAG) promoter was injected unilaterally into the PFC at a volume of 1 μL (0.1 μL/min). Two mice were used and results were highly consistent. In multi-fiber photometry experiments, AAV1-CaMKIIa-GCaMP6f was delivered unilaterally to the PFC and HPC, and AAV1-CAG-GCaMP6f was delivered contra-laterally to the mdTH at a volume of 1.0 μL (0.1 μL/min). After viral delivery, an additional 5-10 min delay was applied to ensure viral spread before slowly removing injection needle. GCaMP6-expressing virus and rgAAV-GFP virus were obtained commercially from the UPenn Viral Core. Custom RNAi and gene expression AAV production was carried out at Vigene Biosciences and Boston Children's Hospital Viral Core, respectively. Viral and tracer coordinates were as follows (in mm): mdTh coordinates: −1.25 A/P, −3.4 D/V, ± 0.4 M/L; PFC coordinates: 1.8 A/P, −1.7 D/V, ± 0.35 M/L; HPC coordinates: −1.5 AP, −1.8 D/V, +1.75 M/L. Coordinates are relative to bregma (A/P, M/L) and to skull (D/V)

In multi-fiber photometry experiments, one week after GCaMP viral injection (coordinates specified in Figure S5B), mice were unilaterally implanted with 1.25 mm ferrule-coupled optical fibers (0.48 NA, 400 μm diameter) immediately dorsal to the targeted structure (mdTh, PFC or HPC), fixed to the skull with dental cement. A light weight titanium head plate implant was used to enable stable head fixation during tethering of the animal to optical patchcords each day.

RNA Expression Analysis

RNA extraction from brain tissues

For tissue extraction, mice were sacrificed by cervical dislocation and immediately decapitated in compliance with IACUC protocol #17002. The targeted brain regions were harvested from 1 mm brain slices (Figure 3A), obtained by brain matrices (ZIVIC) using 1.0 mm tissue punches and transferred to a tube containing 300 μL of ice-cold lysis buffer and 3 μL β-mercaptoethanol (Total RNA Purification kit, NORGEN; following the manufacturer's protocol). Samples were then homogenized by passing a 25G insulin syringe six times and left on ice.For RNA extraction, the total RNA Purification kit was used according to the manufacturer's instructions (NORGEN). RNA quality was evaluated by Bioanalyzer 2100 (Eukaryote Total RNA Nano chip, Agilent) at the Rockefeller University Genomic Resource Center (RIN > = 7.50 and free of genomic DNA contamination). RNA samples were then aliquoted and stored at −80°C.

RNA sequencing (RNA-seq) analysis

For RNaseq, RNA libraries were prepared from 100ng of total RNA per sample for 6 DO mice, 4 brain regions per mouse (Figure 3A) using the TruSeq stranded mRNA LT kit (Cat# RS-122-2101, Illumina). These synthetic RNAs cover a range of concentrations, length, and GC content for validation of the fidelity and dose-response of the library prior to downstream procedures. Libraries prepared with unique barcodes were pooled at equal molar ratios following manufacturer's protocol (Cat# 15035786 v02, Illumina). The pool was denatured and subject to paired-end 50x sequencing on the Hi-Seq 2500 platform. An average of 67 million reads per sample were obtained. Sequencing reads were aligned to the mouse genome (mm10) using STAR (v2.4.2a) and aligned reads were quantified using Salmon (v0.8.2). Approximately 90% of the reads mapped uniquely. Hierarchical clustering and Principal Components Analysis were performed following Variance Stabilizing Transformation (VST) from DESeq2, which is on the log2 scale and accounts for library size differences. The hierarchical clustering heatmap shows the Euclidean distances of VST of the counts between samples.

Quantitative PCR (qPCR)

For quantitative PCR, each reverse transcription was performed with 0.2 μg RNA using the TruScript First Strand cDNA Synthesis Kit (NORGEN), in a final volume of 10 μl. Primers for reverse transcription were equal mixtures of poly-T nucleotides and random hexamers. Negative controls (omitting reverse transcriptase enzyme) were performed for each sample. The cDNA products were diluted 1:10 and 2 μl was analyzed by qPCR using custom primer sets using SYBR Green dye (20 μl total reaction, BioRad). RT-qPCRs were performed on a Lightcycler 480 from Roche. Every reaction was systematically run in triplicate. Conditions were the following: 50°C 2 min, 95°C 10 min, 40 × (95°C 15 s, 60°C 1 min). qPCR Ct values were analyzed using the LightCycler software. Detection threshold was set at ΔRn = 0.3, with this limit always within the 2n exponential amplification phase of genes. Mean of technical triplicate values were reported. All DO mice gene expression Ct values were normalized with the reference gene Ube2d2a using ΔΔCt method to determine the relative mRNA expression of each gene. γTubulin was used as a reference gene to control for potential differences between strains (C57 versus CC012).

siRNA Experiments *In Vitro & In Vivo*

RNAi and gene expression construct

We used the following shRNAs for gene knockdown (which were then subcloned into a pAV-U6-RFP construct, VigeneBiosciences): *Gpr12* (GenBank: NM_008151.3), Targeting sequence: TACATCCAGATTTGTAAGAT; *Tmem130* (GenBank: NM_177735.4), Targeting sequence: AATCTAACCTCGACCATCC; Nptx2 (GenBank: NM_016789), Targeting sequence: CCGTCGTGCAGCAGAAG

Please cite this article in press as: Hsiao et al., A Thalamic Orphan Receptor Drives Variability in Short-Term Memory, Cell (2020), https://doi.org/10.1016/j.cell.2020.09.011

GAGACG. For gene expression, coding sequence of *Gpr12* and *Grid2ip* were cloned from mouse cDNA clone (TrueORF cDNA Clones, OriGene) and subsequently subcloned into a pAAV–hSYN-ires tdTomato expression vector using standard molecular cloning techniques (the C¿ V5-epitope tags in frame with the coding forward-reading frame). Constructs were verified first by Sanger sequencing, and then diagnostics for ITR integrity, by digestion with SmaI, before AAV production.

Western Blot

Protein lysates were prepared from 5-15mg of micro-dissected brain tissue. Tissue samples were homogenized using a 25G syringe in 1.5 ml ice-cold lysis buffer containing 1% protease inhibitor cocktail and phosphatase inhibitor (ProteoExtract Cat#71772-3, Calbiochem) and kept at 4°C for 40 min before the cytosolic fraction was removed by centrifugation at 5,000 g for 10 min. The pellet was resuspended in 0.2 mL Extraction Buffer containing 2% protease inhibitor cocktail and incubate for 45 min with gentle agitation. Debris were removed by 16,000 g centrifugation and the supernatant, which is enriched in membrane proteins was either stored or mixed with 50% 2x LDS sample buffer (#NP0007; Thermo Fisher Scientific) containing 50 mM dithiothreitol (DTT) and boiled at 70 °C for 10 min. 30 μg of protein per sample was used in the case of mediodorsal thalamus lysates to evaluate Gpr12 expression (Figure S4D); 50 μg of protein was used in the case of HT-22 isolations (Figure S4I). Using SDS polyacrylamide gels (12% or 8%–16%), we separated samples via electrophoresis with Tris–glycine buffer (25 mM Tris base, 192 mM glycine, 0.1% SDS) and transferred onto nitrocellulose or PVDF membranes (0.45 μm; Millipore) with Towbin buffer containing 25 mM Tris base, 192 mM glycine and 20% methanol using a wet transfer system (Bio-Rad) with the following settings: 25 V maximum overnight. After transfer, membranes were washed with water and air-dried, followed by blocking membranes in 5% skim milk/TBS for 30 min at room temperature and blocking for further 30 min in fresh solution. Incubation with primary antibody was performed overnight on a shaker (60 rpm) at 4 °C in 3% skim milk/TBST (0.1% Tween 20 in TBS) using the following antibodies: rabbit anti-Gpr12 (AVIVA, Cat#ARP64695; 1:1,000) and anti-Tubulin (Covance, Cat#MMS-435P; 1:2,000). Membranes were washed three times in TBST at room temperature on a shaker (60 rpm) for 10 min, followed by a 2-h incubation of 1:15,000 goat anti-rabbit secondary antibody conjugated with AlexaFluor 780 or 1:20,000 goat anti-mouse secondary antibody conjugated with AlexaFluor 680 (LI-COR) in 3% skim milk/TBST on a shaker (60 rpm) at room temperature. For quantification, samples were run as biological replicates on one membrane, and the mean was further used for graphs and statistics, with the exception of Figure S4I, where samples were run as duplicates. Non-saturated images were used and analyzed with Image Studio Lite software (LI-COR).

In Situ *Hybridization*

The hybridization protocol used in the present study was adapted from the HCR v3.0 Molecular Instruments protocol (Choi et al., 2010). After perfusion, brains were kept in 4% PFA overnight, then transferred to 30% sucrose overnight, both times at 4°C on a nutator. Brains were sliced to 45 μm thickness using a microtome. Brain slices were prehybridized in 500 μL probe hybridization buffer (Molecular Instruments) for 30 min at 37°C. Slices were then incubated in probe solution (Molecular Instruments) containing 12 nM of probe of interest overnight at 37°C on a nutator. The next day, slices were rinsed 4x15 min with probe wash buffer at 37°C (Molecular Instruments) and 3 × 5 min with 5X saline sodium citrate with 0.1% Tween-20 (SSCT) at room temperature. Slices were then pre-amplified in 500 μL of amplification buffer for 30 min at room temperature on a nutator and transferred to hairpin mixture solution containing 60 nM of both snap-cooled hairpin 1 and hairpin 2 (Molecular Instruments); slices were incubated overnight in the dark at room temperature on a nutator. The next day, slices were rinsed with 5X-SSCT for 2 × 5 min and 2 × 30 min at room temperature. Slices were then mounted on glass slides (ProLong Diamond- Invitrogen mounting media).

Histology & Immunohistochemistry

Mice were transcardially perfused with PBS and 4% paraformaldehyde in 0.1M PB, then brains were post-fixed by immersion for ~24 h in the perfusate solution followed by 30% sucrose in 0.1M PB at 4°C. The fixed tissue was cut into 40 μm coronal sections using a freezing microtome (Leica SM2010R), stained with DAPI (1:1000 in PBST), and mounted on slides with ProLong Diamond Antifade Mountant (Invitrogen). For immunostaining, the fixed sections were permeabilized with 70% methanol for 15 min before blocking with 5% normal donkey serum in PBS for 1 h and incubated with primary antibodies overnight at 4°C. Sections were washed three times in PBS and incubated with appropriate secondary antibodies overnight at 4°C. Afterward, coverslips were mounted using ProLong Diamond Antifade mounting medium for image collection. Primary and secondary antibodies include rabbit polyclonal anti-Gpr12 (AVIVA, Cat#ARP64695), guinea pig polyclonal anti-Parvalbumin (SWANT, Cat#GP72), mouse monoclonal anti-V5 tag (Invitrogen, Cat# R960-25), mouse monoclonal anti-Tubulin (Covance, Cat#MMS-435P), Alexa Fluor 488 donkey anti-mouse IgG (Jackson ImmunoResearch, Cat# 715-546-150), Rhodamine Red-X donkey anti-rabbit IgG (Jackson ImmunoResearch, Cat# 711-296-152), Alexa Fluor 647 donkey anti-guinea pig IgG (Jackson ImmunoResearch, Cat# 706-606-148), DAPI (Cayman Chemical, Cat#28718-90-3). For immunohistochemistry staining, confocal images were obtained at room temperature on Zeiss LSM 790 at 2,048 × 2,048 pixels using a Zeiss 5 × (NA 0.15, dry), 20x dry objectives with the same settings and configurations for all samples within each experiment.

In Vitro Calcium Imaging

Cell culture and DNA transfection

HT-22 mouse hippocampal neuronal cell lines (Sigma-Aldrich), were maintained in Dulbecco's modified Eagle's medium supplemented with 10% fetal bovine serum, incubated at 37°C in a humidified atmosphere with 5% CO2. For the dual-guide approach, we transfected HT-22 with both *Gpr12* gRNA1 and gRNA2 Cas9 vectors and collected individual HT-22 colonies after puromycin selection (3000 μg/mL). At 24 h after transfection, cells were dissociated and single cells were isolated by fluorescence-activated

Please cite this article in press as: Hsiao et al., A Thalamic Orphan Receptor Drives Variability in Short-Term Memory, Cell (2020), https://doi.org/10.1016/j.cell.2020.09.011

cell sorting (FACS) gated for a high level of RFP expression. Genomic DNAs from individual colonies were screened by PCR for the presence of an expected –0.7-kb junction product (Figure S4F). Complete protein depletion in each target gene was confirmed by Western Blot analyses of clonal cell lines.

Gpr12 Knockout

CRISPR/Cas9-mediated gene targeting was used to deplete *Gpr12* in HT-22 cells. We used the CRISPR Design Tool (https://portals.broadinstitute.org/gpp/public/analysis-tools/sgrna-design) to obtain the sequences of guide RNAs targeting the *Gpr12* Exon2 segment. The design of guide RNAs and reference sequences are *based* on genome assembly GRCm38. We then performed a degenerate BLAST search with all possible guides to identify sequences that would uniquely target Gpr12 locus with no predicted off-target effects. The sequences of dual-guide RNAs were as follows: Gpr12 gRNA1: 5¿- GGGTTGTCTGTCTTTCTCTG; Gpr12 gRNA2: 5¿- GGGTTGTCTGTCTTTCTCTG. *Gpr12* gRNA1 was cloned into pSpCas9(BB)-2A-Puro plasmid with a puromycin resistance marker (pX459, Addgene plasmid 48139) using a BbsI restriction site. Gpr12 gRNA2 was cloned into EF1a-T7-hspCas9-T2A-RFP-H1-gRNA Cloning Vector (SystemBiosciences). Validation of the guide sequence in the Cas9 vectors was confirmed by Sanger Sequencing. Before transfection, all plasmids were purified using EndoFree Plasmid Maxi Kit according to the manufacturer's instruction (QIAGEN).

Neural Differentiation

HT-22 mouse hippocampal neuronal cell line (Signa-Aldrich) as control cells (wildtype) and CRISPR-mediated knockout cells lacking *Gpr12* (deletion mutation c. 96_538del443 at *Gpr12* locus) were grown in Dulbecco's modified Eagle's medium supplemented with 10% fetal bovine serum, 1% penicillin/streptomycin (GIBCO) at 37 °C in the presence of 5% CO2. Cells were differentiated in NeuroBasal medium (Invitrogen) containing 2 mmol/L glutamine and 1 × N2 supplement (Invitrogen) for 24 h. before use. Only cells with passage number < 20 were used. For all imaging studies, cells were plated on black 24 well plate with flat and clear bottom (#1.5 polymer coverslip, ibidi) pre-coated with poly-D-lysine. For overexpression of *Gpr12*, we applied Lipofectamine (Invitrogen)-mediated transfection on wildtype cells with expression vector encoding *Gpr12* (aav-hsyn-Gpr12-iresTdT or pCMV6-Gpr12-iresTdT) for 12 h.

Live-cell Imaging of Ca Transients

Differentiated neuronal cells were loaded with the cytosolic Ca^{2+} indicator, 5 μM Cal520-AM dye (Aat Bioquet) to study cytosolic Ca^{2+} dynamics, in a Ca^{2+}-containing HEPES buffered salt solution (Ca^{2+}-HBSS) composed of (mM): 135 NaCl, 5.4 KCl, 2 CaCl2, 1 MgCl2, 10 HEPES, and 10 glucose; pH = 7.4 in 37°C for 20 min. Following dye loading, cultured plate were perfused with PBS buffer to remove excessive dye for three times prior to imaging. Cells were imaged in Leibovitz's L-15 buffer (with additional 30 mM CaCl2, 2 mM sodium pyruvate, 8 mM glucose and 10 mM sodium HEPES, and no phenol red, pH 7.4; Sigma-aldrich) on a Nikon TiE inverted fluorescence microscope with Perfect Focus mechanism. Intracellular Cal520-AM was illuminated at 488 nm from LED light source. Wide-field fluorescence images were captured with Flur Apo 40X objective and sCMOS camera (Andor Neo) at image size of 1024 × 1024 pixels and an acquisition rate of 4 frames per s. Cells were treated with the excitatory neurotransmitter, 10 mM L-glutamic acid (Sigma-Aldrich), to induce neural activity at either 30 s (Gpr12 overexpression experiments) or 15 s (Gpr12 knockout and calcium channel blockade experiments) during continuous live-cell imaging. Experiments were performed at 37°C in environmental chamber.

In-Vitro Ca Imaging Data Analysis

Image data in NIS-Elements (Nikon) ND2 format were converted into tiff stacks and processed in ImageJ (US National Institutes of Health). Regions of interest (ROIs) were automatically selected from a binary z-projection image for each FOV and the gray value was averaged for each ROI for a given time point. Duplicate, false-positive, and incomplete (i.e., cells at the edges of FOV) ROIs were manually excluded from further analysis. The extracted fluorescence intensity changes were detrended (MATLAB "detrend"). Significant calcium events were defined as those signals that exceed the mean baseline by 2 or more standard deviations (Rajasethupathy et al., 2015) (Gpr12 overexpression experiments). Activity-dependent (ie. Glutamic acid-induced) calcium event amplitudes were expressed as a fluorescence ratio (ΔF/F0) by taking the intensity at the time of peak fluorescence (ΔF) divided by the mean fluorescence (F0) at that pixel averaged over a 100 frame-window surrounding the stimulation event (*Gpr12* knockout and VGCC blockade experiments). Spontaneous activity was defined as the number of time points where signals deviate from the mean baseline by more than one standard deviation during resting state (no glutamic acid stimulation). Same analyses were performed to measure the spontaneous and glutamic acid-induced calcium event aptitudes under different blocker treatment conditions. We performed 4 independent experiments for each treatment condition and Student's t test was used to identify significant differences between control and knockout groups.

In Vivo Multi Site Photometry Recordings

Photometry Setup

A custom multi-fiber photometry setup was built as previously described (Kim et al., 2016), with some modifications that were incorporated to increase signal to noise, detailed below. Excitation of the 470 nm (imaging) and 405 nm (isosbestic control) wavelengths were provided by LEDs (Thorlabs M470F3, M405FP1) which are collimated into a dichroic mirror holder with a 425 nm long pass filter (Thorlabs DMLP425R). This is coupled to another dichroic mirror holder with a 495 nm long pass dichroic (Semrock FF495-Di02-25x36) which redirects the excitation light on to a custom branching fiberoptic patchcord of three bundled 400 μm diameter 0.22NA fibers (BFP(3)_400/440/900-0.22_2m_SMA*-3xFC, Doric Lenses) using a 10x/0.5NA Objective lens (Nikon CFI SFluor 10X, Product No. MRF00100). GCaMP6f fluorescence from neurons below the fiber tip in the brain was transmitted via this same

Please cite this article in press as: Hsiao et al., A Thalamic Orphan Receptor Drives Variability in Short-Term Memory, Cell (2020), https://doi.org/10.1016/j.cell.2020.09.011

cable back to the mini-cube, where it was passed through a GFP emission filter (Semrock FF01-520/35-25), amplified, and focused onto a high sensitivity sCMOS camera (Prime 95b, Photometrics).

The multiple branch ends of the branching fiberoptic patchcord were connected to an array of three fiberoptic rotary joints (FRJ_1x1_FC-FC, Doric Lenses) and coupled to three 1 m low-autofluorescence patchcords (MFP_400/430/1100-0.57_1m_FC-ZF1.25_LAF, Doric Lenses) which is used to collect emission fluorescence from 1.25mm diameter light weight ferrules (MFC_400/430-0.48_ZF1.25, Doric Lenses) using a mating sleeve (Doric SLEEVE_ZR_1.25). The excitation is alternated between 405nm and 470nm by a custom made JK flip flop which takes the trigger input from the sCMOS and triggers the two excitation LEDs alternatively. Bulk activity signals were collected using the PVCAM software, and data were further post-processed and analyzed using custom MATLAB scripts.

Photometry Recordings

Mice performed the delayed to non-matching place (DNMP) task while we recorded bulk calcium signals from three regions, the prefrontal cortex (PFC), hippocampus (HPC) and mediodorsal thalamus (mdTh), simultaneously. We recorded at 15 Hz frequency with excitation alternating between 470 nm (calcium dependent fluorescence) and 405 nm (calcium independent fluorescence) excitation wavelengths, resulting in an effective frame rate of 7.5 Hz, sufficient for capturing GCaMP6f fluorescence dynamics.

QUANTIFICATION AND STATISTICAL ANALYSIS

Behavior Statistical reporting

Sample sizes were selected based on expected variance and effect sizes from the existing literature, and no statistical methods were used to determine sample size *a priori*. Prior to experiments being performed, mice were randomly assigned to experimental or control groups. The investigator was blinded to all behavioral studies (except for CC012 versus C57 cohorts, Figures 2E–2G, where coat color differences prevent blinding during experimentation). Data analyses for calcium imaging (*in vitro* and *in vivo* datasets) were automated using MATLAB scripts. Statistical tests were performed in MATLAB 2017a or Graphpad Prism 7.

Gene Expression Statistics

Differential gene expression between high and low performing DO mice was determined in R (3.5.0) using the DESeq2. P values were determined using a Wald test and p values were corrected using the Benjamini-Hochberg (BH) method.

Multi-Fiber Photometry Data Processing

For analysis, the images captured by the sCMOS camera were post-processed using custom MATLAB scripts. Regions of interest were manually drawn for each fiber to extract fluorescence values throughout the experiment. The 405-nm reference trace was scaled to best fit the 470-nm signal using least-squares regression. The normalized change in fluorescence (dF/F) was calculated by subtracting the scaled 405-nm reference trace from the 470-nm signal and dividing that value by the scaled 405-nm reference trace. The true baseline of each dF/F trace was determined and corrected by using the MATLAB function ‘‘msbackadj’’ estimating the baseline over a 200 frame sliding window, regressing varying baseline values to the window’s data points using a spline approximation, then adjusting the baseline in the peak range of the dF/F signal. Task events (for example, delay phase and arm choices), were time stamped via video based behavioral tracking from EthoVision (Noldus) program, and behavior was video recorded as described above.

Multi-Fiber Photometry Data Analysis

Total mean activity, for different task phases, and different strains, were quantified as area under the curve (AUC) of dF/F responses. To facilitate comparison across mice, dF/F responses were z-scored and shifted above 0. AUC was calculated using MATLAB ‘‘trapz’’ function and normalized with the recorded time.

Pearson Correlation of the dF/F responses was performed between different regions using the ‘‘corr’’ (MATLAB) function. To ensure that correlation values were significantly more than chance, each timeseries was scrambled 10,000 times randomly, for each trial across all mice. All such chance correlation coefficients were pooled to calculate mean and standard deviation of chance correlations. Correlations between different regions may also accrue due to the long responses of photometry signals reflecting bulk neural activity. To control for this, timeseries from each brain region were circularly permuted within each task phase to create an offset of 15-25 frames (selected randomly in each iteration) using the ‘‘circshift’’ function in MATLAB. Correlation coefficients were then calculated by repeating this step 10,000 times for each trial across all trials and mice, and compared with signal correlations.

CellPress

Supplemental Figures

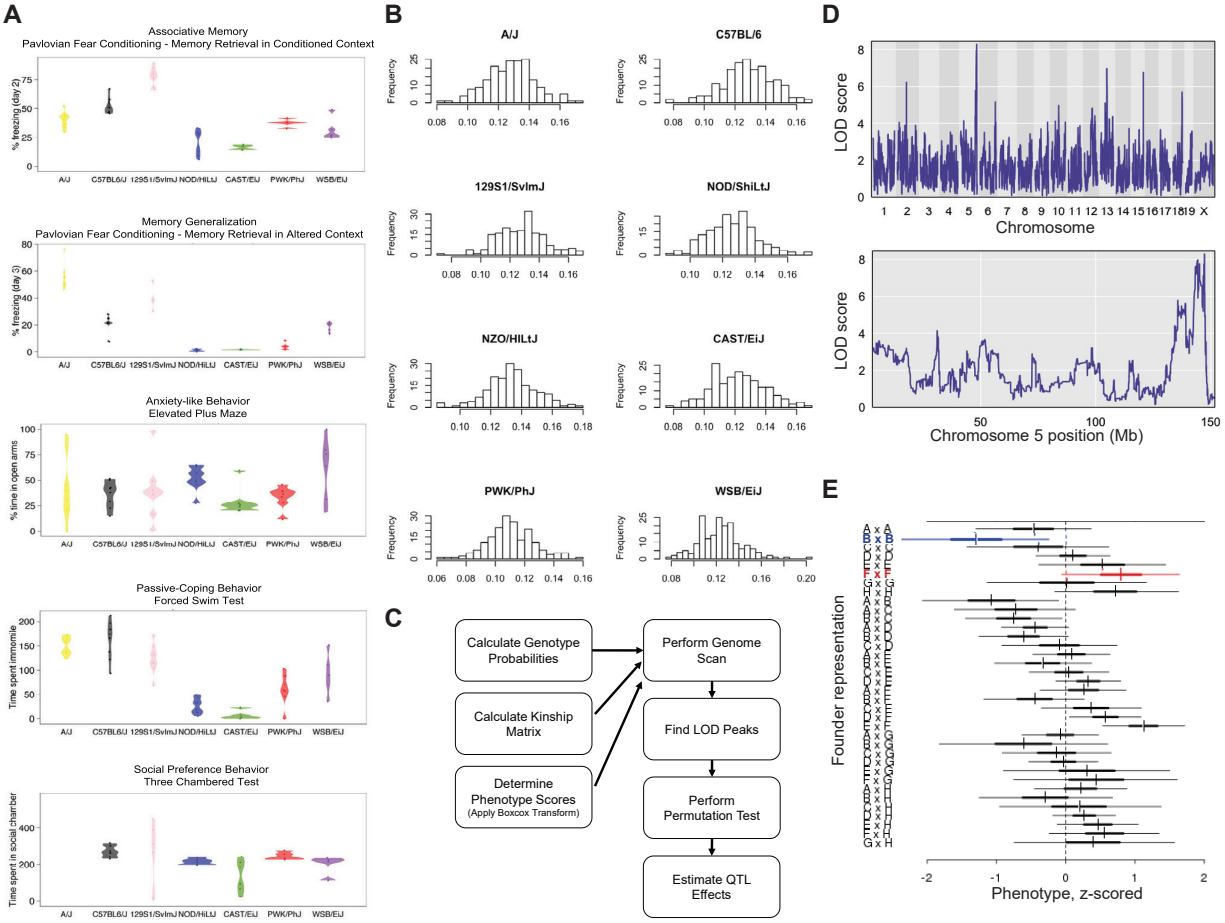

(legend on next page)

Figure S1. Pilot Behavioral Data on Founder Strains and Control Experiments for Haplotype-Specific Phenotypic Variation Associated with *Smart1*, Related to Figures 1 and 2

(A) Behavioral phenotyping of the founder strains (n = 8 ea.) on each of the behavioral tasks indicated in the following order: 1. Fear Conditioning, 2. Memory Generalization, 3. Elevated Plus Maze, 4. Forced Swim, and 5. Three Chambered test. NZO/HiLtJ was not available from The Jackson Laboratory at the time of testing and therefore was not included. Some A/J mice were recovering from aggression wounds at the time of conducting the three chambered test and were not included for that test.

(B) Distribution of alleles inherited from each founder strain for mice in our cohort at DO 25th generation, showing approximately equal contributions.

(C) Workflow for QTL mapping.

(D) Results of mapping analyses performed using R/qtl2 (Broman et al., 2019).

(E) Diplotype effects at *Smart1* locus.

(F and G) The spontaneous alternation performance of the Collaborative Cross strains-tested did not have significant correlations with the number of arm entries made (*left*), or with latency to first arm entry (*right*), or stereotypic movement (*middle*). Correlations (slope of linear regression is non-zero) were Not Significant by t test: p = 0.7688, p = 0.2192, p = 0.6863 respectively for (F); p = 0.6220, p = 0.4025, p = 0.9138 respectively for (G).

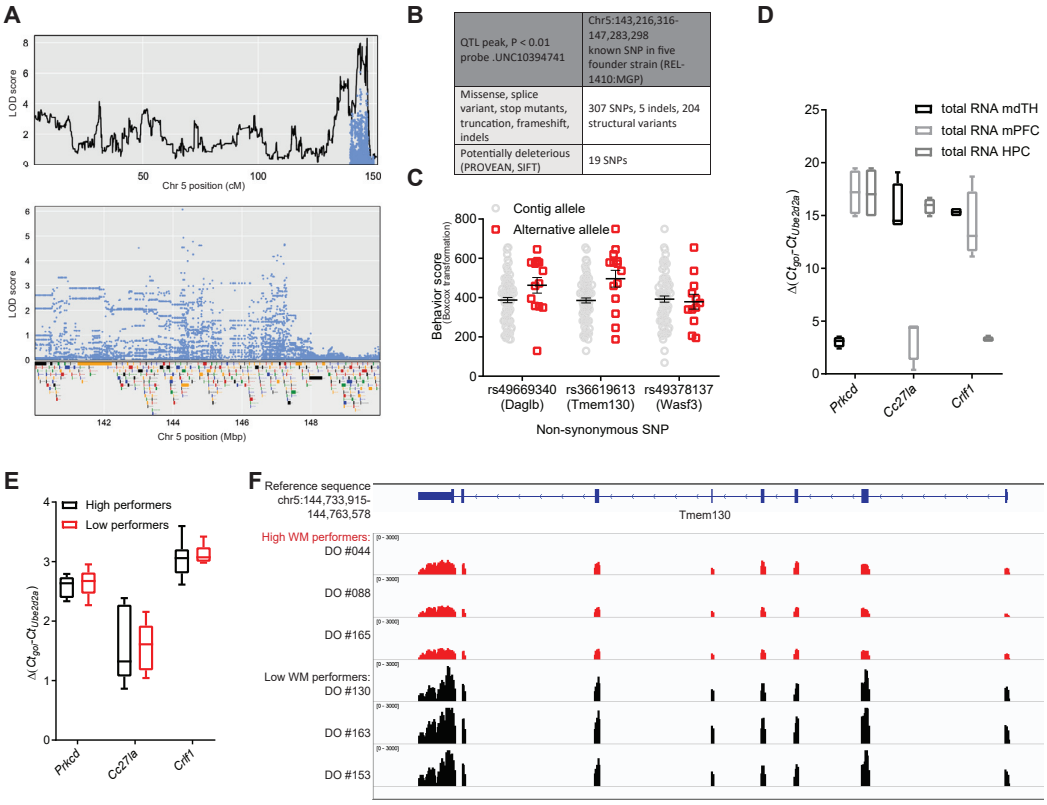

Figure S2. SNP Mapping and Circuit-Specific Gene Expression on Working Memory Performance, Related to Figure 3

(A) SNP association in the QTL peak region.

(B) Workflow for identifying causal SNP variants.

(C) SNPs to phenotype (Boxcox transformation) association for three SNPs in *Smart1* locus using a subset of the DO population (n = 104), in mean ± SEM. Multiple SNPs segregated high and low performers.

(D) qPCR was performed on total RNA extracted from brain regions indicated in (Figure 3A) using *Prkcd*, *Cc27la*, *Crlf1* qPCR probes, selected from the Anatomic Gene Expression Atlas (Lein et al., 2007), that are highly expressed and/or specifically expressed at mediodorsal thalamus, prefrontal cortex, and hippocampus, respectively. n = 4 animals (C57) each brain region each probe.

(E) qPCR validation of dissection accuracy as demonstrated by region-specific gene expression from DO total RNA samples (6 high performers versus 6 low performers).

(F) Example thalamus RNaseq data for *Tmem130* expression displayed graphically in a coverage plot. Tmem130 expresses more in low performing DO mice ((log2FC/adj-P val: −1.04/0.00; in PFC: 0.30/0.19). We decided to test thalamic Tmem130 due to higher expression in thalamus (than PFC) and significant differential expression by RNaseq.

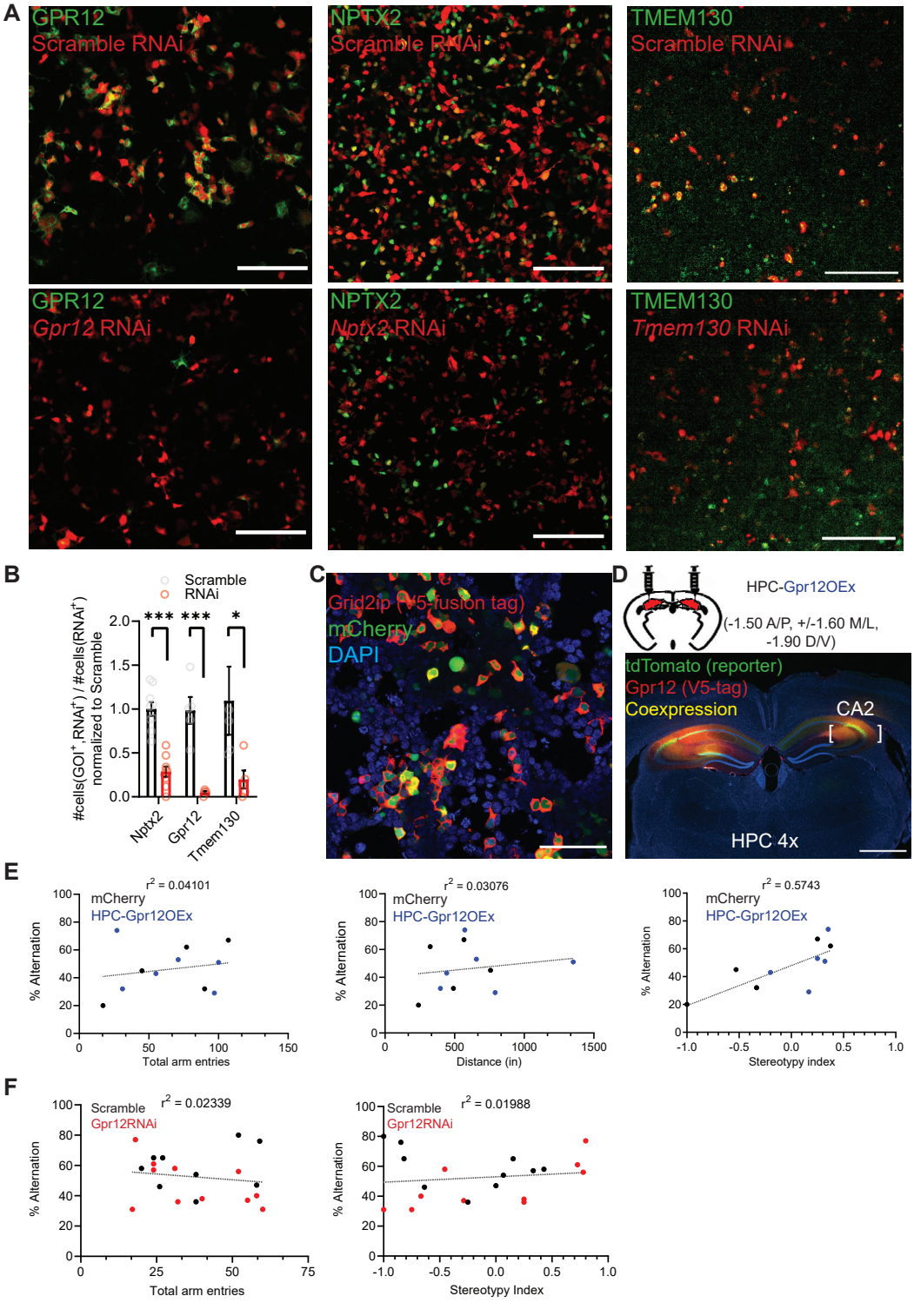

(legend on next page)

Figure S3. Validation of RNA Interference and Gene Expression Constructs and Behavioral Control Experiments for Manipulating Thalamic *Gpr12* Expression, Related to Figure 4

(A) *in vitro* validation of gene knockdown constructs by immunohistochemistry. Wide-field fluorescence image of cells expressing RNAi-mediated gene knockdown construct co-transfected with expression construct for *Gpr12* (scale bar 200 μm), *Nptx2* (scale bar 200 μm), and *Tmem130* (scale bar 100 μm) in HEK cells and visualized with protein fusion tag (green: V5-tag) and transfection marker of either targeted (bottom panels) -, or scrambled (top panels) - RNAi construct (red: mCherry fluorescent protein). Yellow signals indicate co-localization of gene expression in cells with scrambled probe (more apparent in top panels). Red signals indicate lack of co-localization of gene-expression in cells with the RNAi probe (more apparent in bottom panels).

(B) Quantifications of gene knockdown-induced by RNAi are expressed as remaining expression relative to scramble transfected experiment, in mean ± SEM *Nptx2*: 0.286 ± 0.058, n = 9; *Gpr12*: 0.050 ± 0.013, n = 5; *Tmem130*: 0.198 ± 0.103, n = 5 independent experiments.

(C) Gene expression verification for *Grid2ip* construct (Scale bar100 μm).

(D) Histological verification of *Gpr12* viral delivery in hippocampus. Images were acquired and tiled together to generate high-resolution images of whole brain sections.

(E) Animals with AAV viral injection into HPC for overexpression of *Gpr12* demonstrated spontaneous alternation performance that had no significant correlation with the number of arm entries made (*left*), or the distance moved (*middle*); There was significant correlation with Stereotypy (*right*). Correlation (slope = non-zero) t test: p = 0.8724, p = 0.6060, p = 0.5504, **p = 0.0069, respectively; n = 11 animals.

(F) Scramble and Gpr12RNAi injected CC012 mice demonstrated spontaneous alternation performance that had no significant correlation with the number of arm entries made (*left*) or stereotypic movement (*right*). p = 0.5198, p = 0.5532, respectively; n = 20, t test.

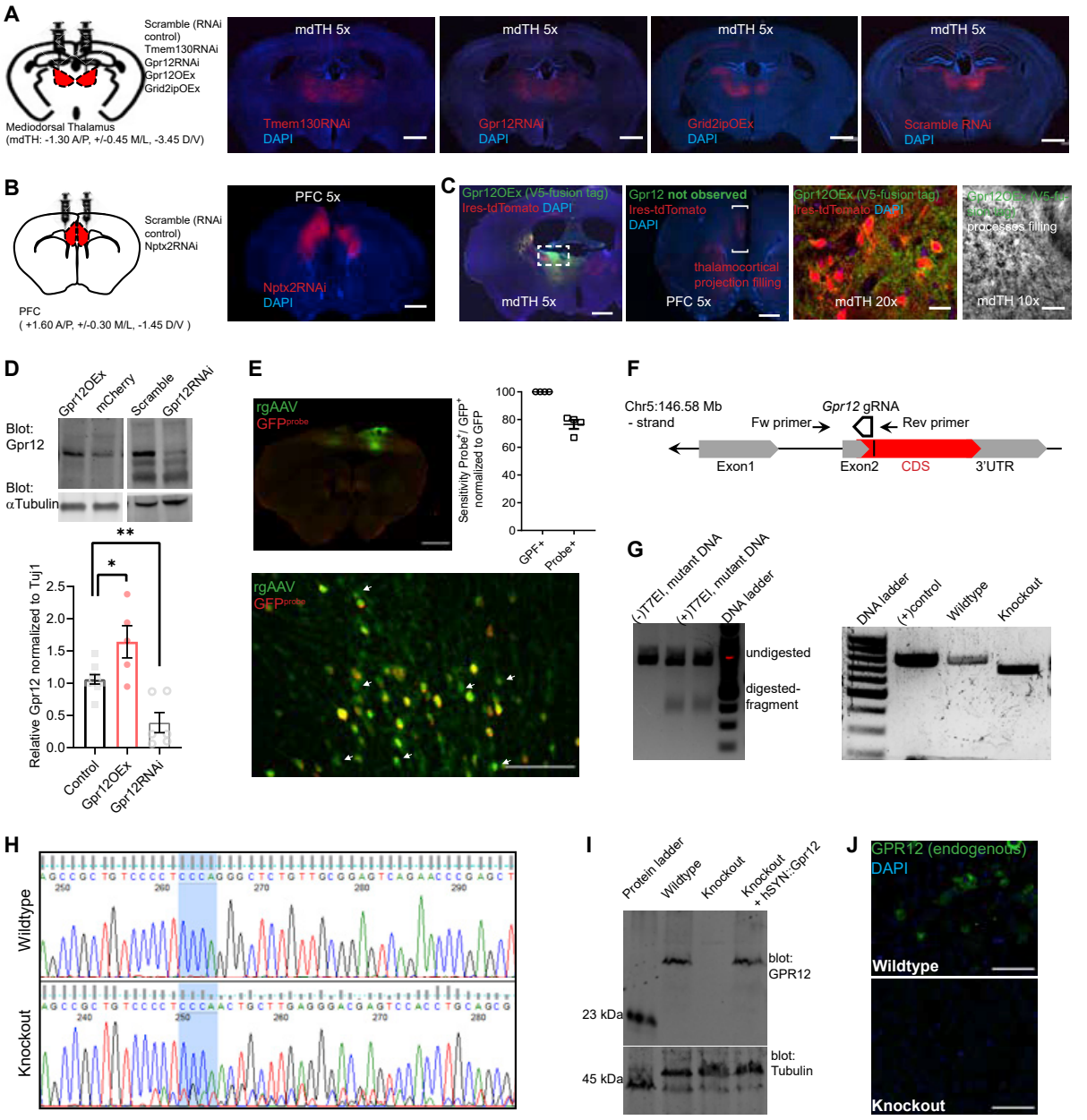

Figure S4. Histological Verification of Viral Delivery in Mouse Brains and Control Experiments for *In Situ* Hybridization and Supporting Data for *In Vitro* Calcium Imaging, Related to Figures 4 and 5

(A and B) Histology performed 8 weeks after injection of viral gene knockdown and expression constructs into the mediodorsal thalamus (A, coordinates specified) and PFC (B, coordinates specified). Viral transduced neurons were detected in targeted brain regions. Scale bars: 1mm; DAPI, 49,6-diamidino-2-phenylindole; mdTH, mediodorsal thalamus ; PFC, prefrontal cortex.

(C) Histology performed 8 weeks after injection of AAV9-hSYN-Gpr12iresTdTomato into the mediodorsal thalamus showing GPR12 localized predominantly to soma and dendrites (not axon terminals in PFC). Virally transduced neurons were visualized in the targeted brain region (dashed square region magnified in panels to the right) and high resolution images showed subcellular GPR12 distribution, green (process filled GPR12 fusion V5, *top left*) versus red (cell filling tdTomato, *bottom left*). Left: 5X; scale bar, 1mm. Right: 10X; scale bar, 100 μm. *bottom*: 20X; scale bar, 40 μm. Images were acquired and tiled together to generate high-resolution images of whole or part of brain sections. The acquired images were processed using the NIS-Elements (Nikon).

(legend continued on next page)

(D) western blot for GPR12 performed 8 weeks after AAV-based overexpression (*left* panel, blotted on nitrocellulose membrane) or knockdown (*right* panel, blotted on PVDF membrane).. Quantifications of viral-mediated gene expression or knockdown-induced by RNAi are normalized to control (ie. Scramble RNAi and mCherry) experiments in mean ± SEM. Gpr12OEx: 1.642 ± 0.249, n = 5, *p = 0.023; Gpr12RNAi: 0.388 ± 0.156, n = 6, **p = 0.006, One-way ANOVA.
(E) HCR *in situ* for GFP as positive control, and to assess sensitivity & specificity of labeling. ISH performed 2 weeks after rgAAV-GFP injection to PFC (*top*; injection coordinates: −1.8 A/P, +0.3 M/L, −1.7 D/V; scale bar: 1mm) and retrogradely labeled thalamocortical projection neurons were detected in mediodorsal thalamus (*bottom*; green: rgAAV GFP label, red: HCR GFP probe; scale bar: 200 μm). Quantifications of labeling sensitivity was expressed in ratio of cell counts of positive control probe labeling / rgAAV GFP labeling, relative to 1. Mean ± S.E.M, sensitivity = 76.50 ± 3.227 (%), n = 4 FOV. Images were collected with × 5 or × 40 objectives and tiled together to generate high-resolution images of brain sections. The acquired images were processed using the Zen (Zeiss).
(F) Schematic of genomic structure of *Gpr12* and CRISPR-mediated gene silencing (*top*).
(G) DNA gel demonstrating T7 Endonuclease I (T7E1) assay of *Gpr12* guide RNA efficiency (*left*) and genomic lesion at *Gpr12* locus in mutant HT22 line (*right*). In left panel, Lane 1: DNA transfected with Cas9 and gRNA, Lane 2 & 3: DNA transfected with Cas9 and guide RNA and digested with T7E1, Lane 4: DNA ladder. In right panel, DNA gel demonstrating a lesion of ~50 bp deletion using PCR primer set surrounding gRNA target site (primer forward: 5¿-AAGTGTGC GAGTGTGCATGT, reverse: 5¿-GTGGTACGTCAGGGCGTAAT). Lane 1: DNA ladder, Lane 2 & 3: PCR control of wildtype alleles, Lane 4: reduced PCR amplicon size of knockout alleles.
(H) Electropherogram of *Gpr12* knockout cell line in order to detect gene deletion. The shaded area indicates the DNA junction before detected deletion in gDNA.
(I) Gpr12 antibody validation with western blot of lysates of wildtype and Gpr12 knockout HT-22 lines showing depletion of GPR12 protein in CRISPR-mediated Gpr12 knockout culture (knockout); representative experiment (n = 2). (F) GPR12 immunohistochemistry in wildtype and *Gpr12* knockout HT22 lines. Scale bar: 50 μm.

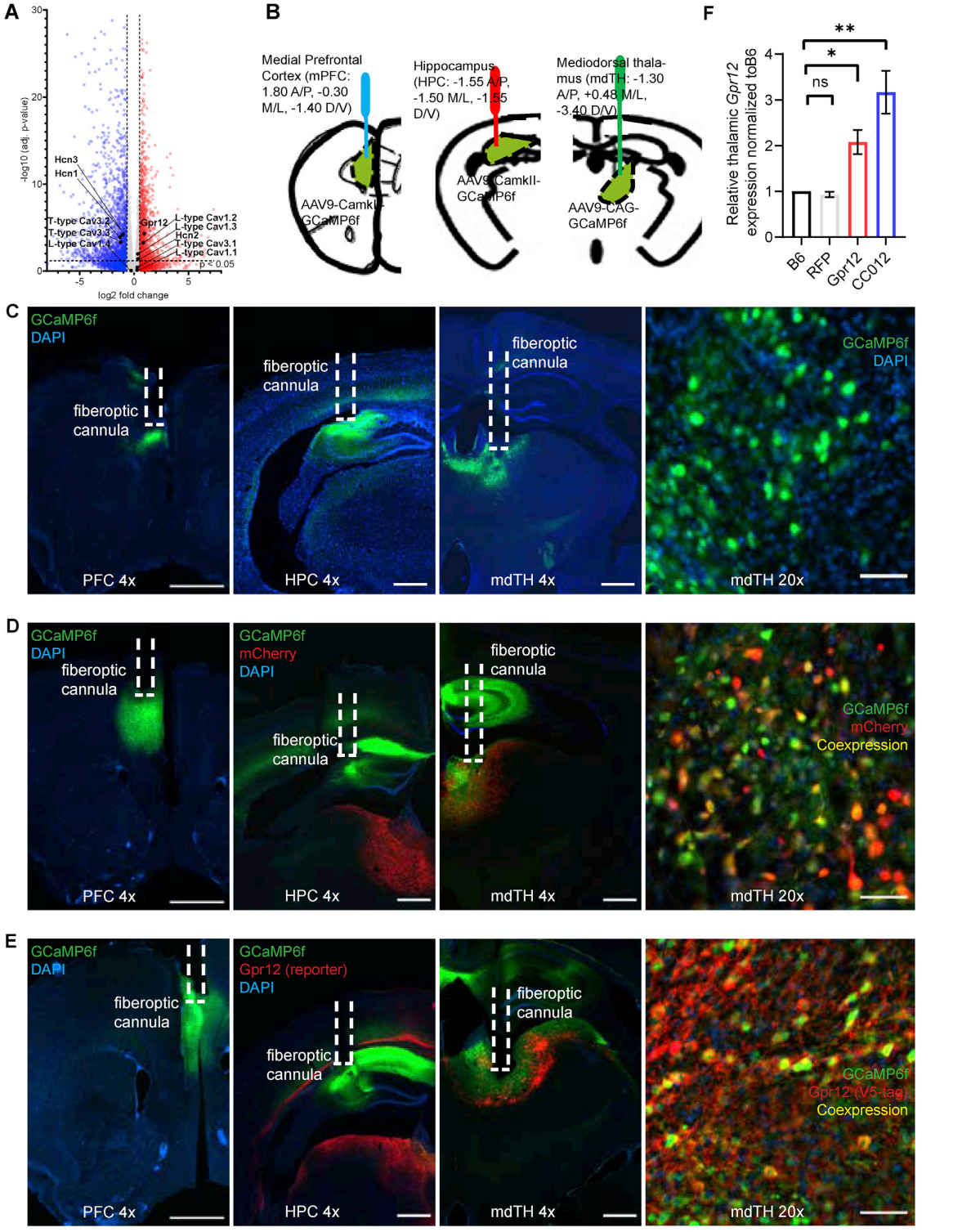

(legend on next page)

Figure S5. Supporting Data for Multi-fiber Photometry Recordings, Related to Figure 6

(A) Volcano plot showing the significance and p value distribution after differential gene expression analysis of the high versus low performers DO mice. Red if they are upregulated and blue if they are downregulated in high performers. Black dots highlight *Gpr12* and calcium channels with expression in mediodorsal thalamus. n = 6 biologically independent samples.

(B) Schematics of multi-fiber photometry viral injection/fiberoptic implantation and coordinates.

(C–E) Representative images of CC012 v B6 (C) and Gpr12 v RFP (D and E) cohorts' histology performed 6 weeks after injection/surgical implantation showing implant above GCaMP6f-expressing neurons (*right* panels, Scale bar, 500 μm). Cell resolution image shows adequate GCaMP6 alone expression (C), GCaMP6 and mCherry co-expression (D), or GCaMP6 and exogenous *Gpr12* co-expression (E) at neuronal cell bodies of mediodorsal thalamus (*right* panels, Scale bar, 50 μm). Images were acquired and tiled together to generate high-resolution images of brain sections.

(F) Gpr12 levels in mediodorsal thalamus tissue from respective behavioral cohorts were measured by qPCR relative to B6 mice. Values and error bars reflect the mean ± SEM of n = 4 independent biological replicates; p(Rfp) = 0.995, *p(Gpr12) = 0.033, **p(CC012) < 0.001.

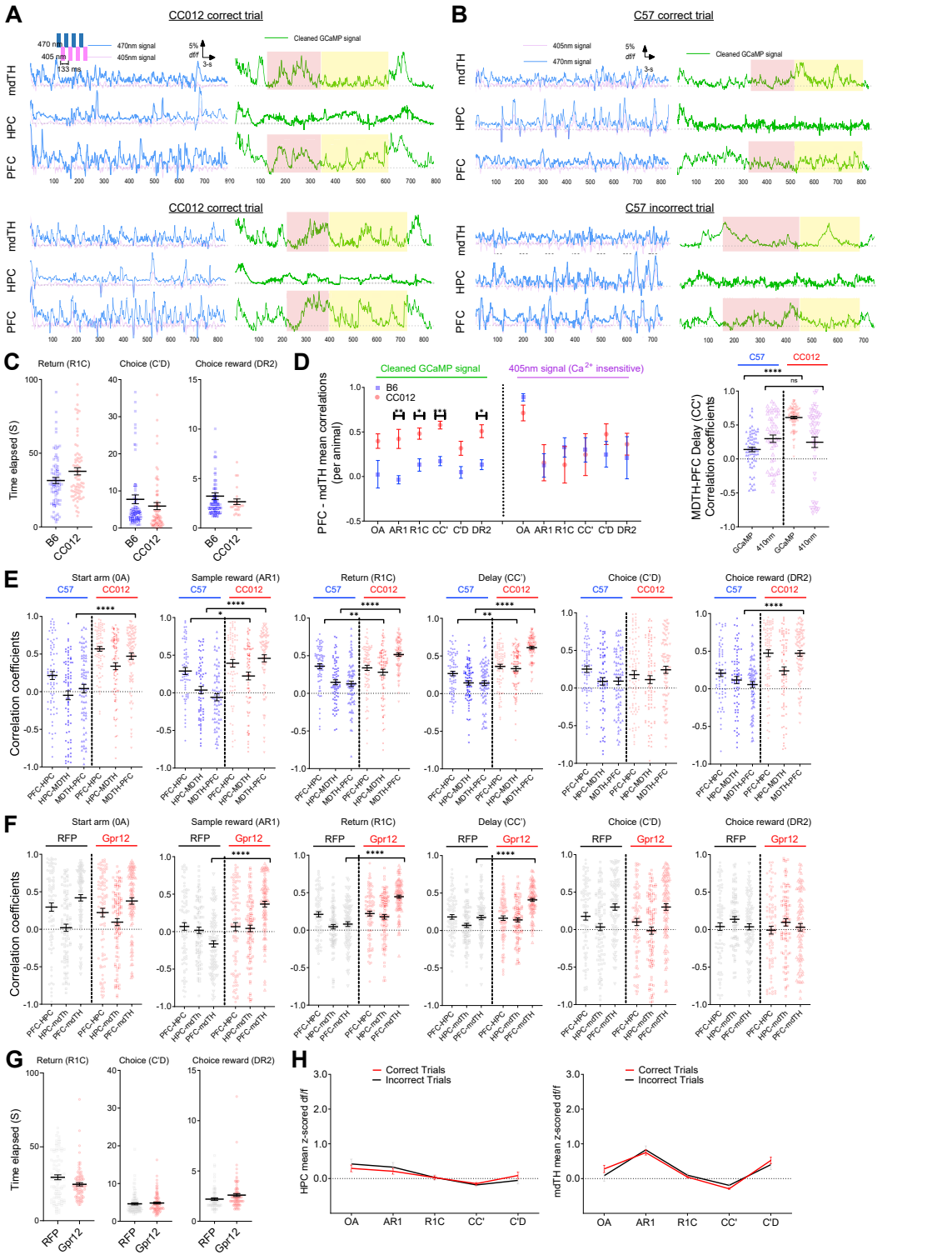

(legend on next page)

Figure S6. Supporting Data for Multi-fiber Photometry Recordings, Related to Figure 6

(A and B) Example traces of two correct trials from CC012 mice (A) and one correct and one incorrect trial from B6 mice (B) during DNMP. The diagram at the top left indicates procedure of simultaneous recording of GCaMP6 at 470 nm and 410 nm (isobestic baseline). Shown are fluorescence traces (df/f) of simultaneously acquired 480 nm signal in cyan (includes calcium sensitive and calcium insensitive signals), 410 nm signal in violet (calcium-insensitive signals only) and cleaned GCaMP signal in green (calcium sensitive signals only) from a freely moving mouse (Methods); pink shaded regions indicate return from choice and yellow shaded regions indicate delay phase.

(C) Time spent in DNMP task phases for C57 and CC012: return (R1C), choice (C'D), and choice reward (DR2) between mouse strains. No significant differences, Unpaired t test. Data are mean ± SEM

(D) Left panel shows Pairwise Pearson's Correlations between mediodorsal thalamus and PFC recordings using the calcium-sensitive signal and the calcium-insensitive signal (410 nm) during each task phase for C57 (blue) and CC012 (red). Data points represent correlation mean across animals, for each strain n = 7 mice, including mean ± SEM 410nm recordings show no significant correlation. Significance found in PFC-mdTH mean correlations: **p(GCaMP) = 0.009 for AR1, *p(GCaMP) = 0.025 for R1C, ***p(GCaMP) < 0.001 for CC' and *p(GCaMP) = 0.016 for DR2 by Two-way ANOVA with Repeated-measure and Sidak's Multiple Comparisons Test. Right panel shows trial-based average mdTH-PFC correlation at the delay phase (CC') at DNMP task.

(E) Pairwise Pearson's Correlations during each task phase for C57 and CC012, individual data point represents mean correlation obtained from one animal, for each strain n = 7 mice, 10 trials per mouse, including mean ± SEM. Significance found in PFC-mdTH mean correlations: **p = 0.009 for AR1, *p = 0.025 for R1C, ***p < 0.001 for CC' and *p = 0.016 for DR2 by Two-way ANOVA with Repeated-measure and Sidak's Multiple Comparisons Test.

(F) Pairwise Pearson's Correlations during each task phase for mediodorsal thalamus viral delivery of Gpr12 or mCherry (RFP), individual data point represents correlation mean of one animal, for each group n = 8 mice, 10 trials per mouse, including mean ± SEM. Significance found in PFC-mdTH mean correlations: **p = 0.002 for AR1, **p = 0.001 for R1C, **p = 0.004 for CC', by Two-way ANOVA with Repeated-measure and Sidak's Multiple Comparisons Test.

(G) Time spent in task phases for Gpr12 v RFP cohort. No significant differences, Unpaired t test. Data are mean ± SEM

(H) Averaged z-scored HPC GCaMP6f (*left*) and mediodorsal thalamus (*right*) activity on correct and incorrect trials. Data are mean ± SEM. No significant differences, Sidak's multiple comparisons test.